Atmospheric Conditions during the Arctic Clouds in Summer Experiment (ACSE): Contrasting Open Water and Sea Ice Surfaces during Melt and Freeze-Up Seasons

Georgia Sotiropoulou,[a] Michael Tjernström,[a] Joseph Sedlar,[a] Peggy Achtert,[b]
Barbara J. Brooks,[c] Ian M. Brooks,[b] P. Ola G. Persson,[d,e] John Prytherch,[b]
Dominic J. Salisbury,[b] Matthew D. Shupe,[d,e] Paul E. Johnston,[d,e]
and Dan Wolfe[d,e]

[a] Department of Meteorology, and Bolin Centre for Climate Research, Stockholm University, Stockholm, Sweden
[b] School of Earth and Environment, University of Leeds, Leeds, United Kingdom
[c] National Centre for Atmospheric Science, University of Leeds, Leeds, United Kingdom
[d] NOAA/Earth System Research Laboratory, Boulder, Colorado
[e] Cooperative Institute for Research in the Environmental Sciences, University of Colorado Boulder, Boulder, Colorado

ABSTRACT

The Arctic Clouds in Summer Experiment (ACSE) was conducted during summer and early autumn 2014, providing a detailed view of the seasonal transition from ice melt into freeze-up. Measurements were taken over both ice-free and ice-covered surfaces near the ice edge, offering insight into the role of the surface state in shaping the atmospheric conditions. The initiation of the autumn freeze-up was related to a change in air mass, rather than to changes in solar radiation alone; the lower atmosphere cooled abruptly, leading to a surface heat loss. During melt season, strong surface inversions persisted over the ice, while elevated inversions were more frequent over open water. These differences disappeared during autumn freeze-up, when elevated inversions persisted over both ice-free and ice-covered conditions. These results are in contrast to previous studies that found a well-mixed boundary layer persisting in summer and an increased frequency of surface-based inversions in autumn, suggesting that knowledge derived from measurements taken within the pan-Arctic area and on the central ice pack does not necessarily apply closer to the ice edge. This study offers an insight into the atmospheric processes that occur during a crucial period of the year; understanding and accurately modeling these processes is essential for the improvement of ice-extent predictions and future Arctic climate projections.

1. Introduction

The Arctic is warming faster than the global climate, a phenomenon widely known as Arctic amplification (Serreze and Francis 2006; Serreze and Barry 2011). While boundary layer processes, and their impact on Arctic warming have received wide attention (Bintanja et al. 2011, 2012; Lampert et al. 2012; Pithan and Mauritsen 2014; Pithan et al. 2014; Vihma et al. 2014), errors in the representation of the Arctic lower atmosphere in climate and weather forecast models (Medeiros et al. 2011; de Boer et al. 2014; Barton et al. 2012, 2014; Wesslén et al. 2014), low-level clouds (Tjernström et al. 2008; Karlsson and Svensson 2013; Sotiropoulou et al. 2016), and surface fluxes (Tjernström et al. 2005, 2008; Svensson and Karlsson 2011) make additional observational studies necessary to improve scientific understanding and, hence, predictive capabilities of the Arctic climate.

Limited understanding of processes important for Arctic climate change is mainly due to a paucity of detailed observations over the Arctic Ocean. A few Arctic campaigns were conducted during the 1970s and 1980s, such as the Arctic Ice Dynamics Joint Experiment (AIDJEX; Bjornert 1975), the Marginal Ice Zone Experiment (MIZEX-83 and MIZEX-84–87; Johannessen 1987; Guest and Davidson 1988) and the Coordinated Eastern Arctic Experiment (CEAREX; Johannessen and Sandven 1989). More detailed information comes from more recent expeditions, which included more extensive suites of instrumentation: the Surface Heat Budget of the Arctic Ocean (SHEBA; Uttal et al. 2002),

Corresponding author address: Georgia Sotiropoulou, Dept. of Meteorology, Stockholm University, Arrhenius Väg 16C, SE-106 91 Stockholm, Sweden.
E-mail: georgia@misu.su.se

the Arctic Ocean Experiment 2001 (AOE-2001; Tjernström et al. 2004), and the Arctic Summer Cloud Ocean Study (ASCOS; Tjernström et al. 2012). Additional information comes from airborne observations, operating from land: the Mixed-Phase Arctic Cloud Experiment (M-PACE; Verlinde et al. 2007); the Arctic Study of Aerosol, Clouds and Radiation (ASTAR 2007; Ehrlich et al. 2008); the Indirect and Semi-Direct Aerosol Campaign (ISDAC; McFarquhar et al. 2011); and the Vertical Distribution of Ice in Arctic Mixed-Phase Clouds (VERDI; Klingebiel et al. 2015). Longer-term data streams come from a set of permanent observatories (Shupe et al. 2011), all land based, and from satellites (e.g., Devasthale et al. 2012; Stroeve et al. 2014).

SHEBA data are still widely analyzed today because of the detailed observations of the surface energy budget and cloud–atmosphere interactions over a full annual cycle; however, these observations were made nearly 20 yr ago in a climate system that has changed vastly since then. Over the last decades the Arctic has experienced considerable changes in ice cover and a substantial warming (e.g., Jeffries and Richter-Menge 2015). The current Arctic climate is now often referred to as "the new Arctic" (Carmack et al. 2015), with substantially reduced and thinner sea ice. These changes accentuate the gap in detailed Arctic process observations, especially in seasonal transitions and in the transition between open water and sea ice.

Summer and early autumn are crucial seasons, corresponding to the sea ice melt period and the beginning of the freeze-up. With increasing areas of open water in summer there is also a growing interest in processes related to the marginal ice zones (MIZ) and in newly formed ice. Sea ice and open water surfaces are expected to have significantly different impacts on lower-atmosphere structure. Enhanced fluxes from the open ocean contribute to a warmer well-mixed boundary layer (Pinto and Curry 1995), potentially altering Northern Hemisphere weather patterns in subsequent seasons (Francis and Vavrus 2015).

Here, we investigate processes determining lower-atmosphere and cloud structure. Using observations from the Arctic Clouds in Summer Experiment (ACSE; Tjernström et al. 2015), we analyze these impacts by segregating observations into different surface conditions (ice and open water), as well as seasons, transitioning from summer melt to autumn freeze-up.

2. Data and methods

a. Arctic Clouds in Summer Experiment

ACSE was a subprogram of the Swedish–Russian–U.S. Arctic Ocean Investigation of Climate–Cryosphere–Carbon Interactions (SWERUS-C3) expedition. ACSE's objectives were to study Arctic clouds and their interactions with boundary layer structure and the ocean surface during the melt and early freeze-up seasons, along with the influence of larger-scale atmospheric dynamics. It was conducted on the Swedish research icebreaker *Oden*, leaving Tromsö, Norway, on 5 July 2014, crossing the Kara, Laptev, East Siberian, and Chukchi Seas, following the Siberian Shelf, and arriving in Barrow, Alaska, on 18 August. A second leg left Barrow on 21 August following a similar route back, albeit farther north. The expedition ended on 5 October, when *Oden* arrived back in Tromsö. The expedition cruise track is displayed in Fig. 1.

The *Oden* is a polar-class icebreaker (class: GL 100 A5 ARC3) capable of continuously breaking ~2-m thick ice at a speed of 3 knots (kt; $1\,kt \approx 0.51\,m\,s^{-1}$). Maneuvering, and using bow thrusters and healing, it can easily break even thicker ice. While operating in ice, a range of sea ice conditions were encountered: from thick multiyear ice, especially during the first leg (Fig. 1a), over broken up melting ice to thin newly formed ice, especially during the second leg (Fig. 1b). Although continuous ice-thickness measurements were not performed, the ice conditions sampled were reasonably representative for the seasons and the year.

ACSE included an extensive suite of in situ and remote sensing instrumentation (Tjernström et al. 2015), largely following the design from ASCOS (Tjernström et al. 2014). Vertical atmospheric structure was measured with radiosondes (Vaisala model RS92) with ~10-m vertical resolution, 4 times daily (341 profiles in total). Cloud properties were observed with a vertically pointing, motion-stabilized 94-GHz (W band) Doppler cloud radar (Moran et al. 2012) with the first radar gate at 65 m and a vertical resolution of 30 m. A combination of measurements from cloud radar, a motion-stabilized scanning Doppler lidar (Achtert et al. 2015), and multiple laser ceilometers were used to determine cloud boundaries. Cloud cover was provided by a ceilometer (Vaisala model CL51; see the user's guide for a description of the algorithm). A visibility sensor (Vaisala model FD12P) and digital imagery from cameras directed off the bow, port, and starboard were useful to separate fog from clouds.

Surface temperature T_{sfc} was measured with two independent, downward-looking infrared radiation temperature sensors (Heitronics model KT15-II) with a resolution of 0.03°C and an absolute accuracy of ±0.5°C. Seawater salinity was measured with a Seabird conductivity, temperature, and depth (CTD) sensor in the seawater intake, ~8 m below the surface. A heated sonic anemometer (Metek model USA-1) and temperature
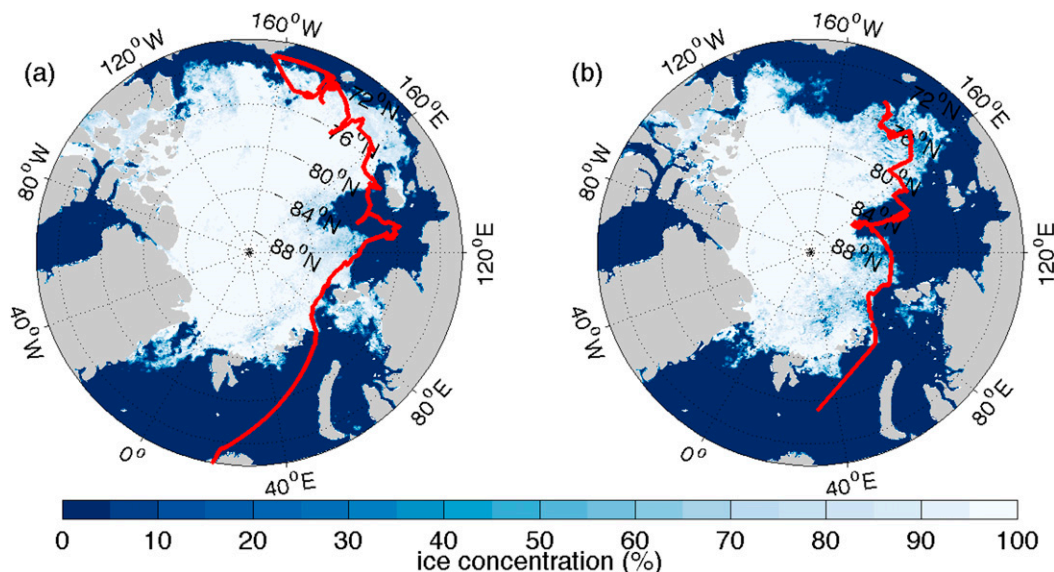
FIG. 1. AMSR2 daily sea ice concentrations for (a) 10 Jul 2014 and (b) 2 Sep 2014. Red lines represent the expedition track for the (a) melt and (b) freeze-up season.

and humidity sensors (aspirated Rotronic and LI-COR model 7500) were deployed $\sim$20 m above the surface on a mast at the bow of the ship; these sensors were used to obtain the turbulent surface fluxes through the eddy-covariance technique. The 10-m equivalent neutral wind speed U_{10N} is derived using the Businger–Dyer stability functions from the 20-m wind speed measurements. A weather station on the seventh deck at $\sim$25 m measured standard meteorological variables: pressure P, temperature T, and relative humidity (RH) (Vaisala model PTU300); wind speed U and direction (Gill WindSonic, heated); and broadband downwelling short- and longwave radiation fluxes [Eppley Standard Precision Pyranometer (SPP) and Precision Infrared Radiometer (PIR)].

One great challenge with shipborne measurements is the elimination of biases and random errors induced by the ship's motion, especially the high-frequency motions due to ice breaking or ocean waves. Both radar and lidar were installed on motion-stabilization platforms, minimizing the impact of the constantly changing motion and orientation of the ship. Lidar winds showed good agreement with radiosoundings (Achtert et al. 2015), indicating the efficiency of the stabilization. An additional challenge is that wind measurements in the lowest atmosphere are affected by flow distortion imposed by the ship's superstructure. To deal with this, a computational fluid dynamics (CFD) study of the flow over *Oden* was undertaken to determine corrections for the wind measurements (Moat et al. 2015). The turbulence measurements were also corrected for ship motion using data derived from a motion sensor collocated with the

sonic anemometer on the mast (Edson et al. 1998; Prytherch et al. 2015).

b. Analysis methods

We separate the data into two seasons, based on lower-atmospheric thermal structure (Fig. 2). The lower troposphere, below $\sim$5 km, was relatively warm until 1200 UTC 27 August, with several warm-air intrusions; the warmest occurring 29 July–8 August was discussed in Tjernström et al. (2015). Following a warm-air pulse on 27 August, the atmosphere abruptly became substantially cooler in a deep layer through the lowest kilometers (Fig. 2a). Prior to 1200 UTC 27 August, the temperature at the base height of the main inversion T_{zi}, referring to the strongest temperature inversion, fluctuated around 0°C, with brief periods of lower values (note that low T_{zi} values may occur also in warm conditions, with high inversion; e.g., during summer $T_{zi} < -7$°C corresponds to inversion-base heights >2 km). After this time, T_{zi} remained considerably lower, but with infrequent increases to near 0°C (Fig. 2b). The mean (median) T_{zi} for the period prior to 1200 UTC 27 August was -0.7°C (-0.2°C), while for the following period it was -10.2°C (-9.4°C). We consider the first period as the summer "melt" season (58% of ACSE duration), whereas the latter is referred to as the autumn "freeze-up."

We also segregate data based on surface state. The classification of surface conditions as open water or sea ice is derived from several sources: T_{sfc} measurements, supplemented by Advanced Microwave Scanning Radiometer (AMSR2) and Special Sensor Microwave
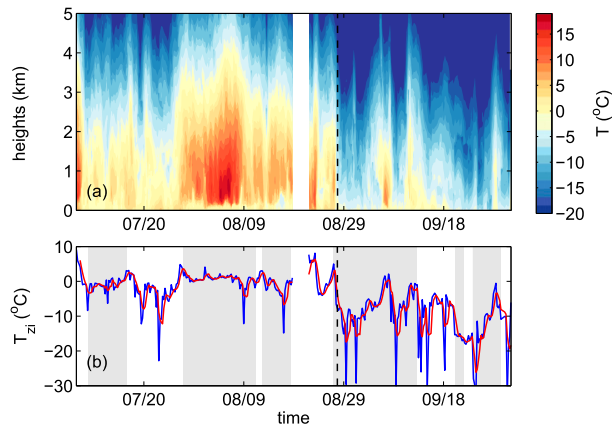
FIG. 2. (a) Time–height cross section of radiosonde temperature profiles T (°C). (b) Time series of the temperature of the main inversion base T_{zi} (°C) from 6-hourly profiles (blue) and daily running means (red). Shading in (b) indicates ice-covered surfaces. The gap shown in both panels corresponds to the rotation period in Barrow (see section 2a). The vertical dashed line separates the melt and freeze-up seasons.

Imager/Sounder (SSMIS) satellite-derived ice concentrations (Kaleschke et al. 2001; Spreen et al. 2008) and webcam imagery. Comparing T_{sfc} to the seawater freezing point T_{freeze}, derived using 8-m salinity, indicates the local-scale state of the surface. However, ice melt and river runoff contribute to freshening of the surface water; cloud precipitation may further enhance the accumulation of freshwater on the ocean surface. In such cases, the 8-m salinity cannot be used to determine the state of the surface, since water will be able to freeze at higher temperature than saline water; freshwater freezes at 0°C; measured T_{freeze} was between $-1°$ and $-1.9°$C, with a mean at $\sim-1.6°$C. Hence, for a more accurate assessment, a combination of all three datasets is used. Note that satellite products have a 6.25-km horizontal resolution, whereas scales derived from camera images correspond to a maximum of ~1 km.

Initially, if ice concentration (n_{ice}) $> 40\%$ and $T_{sfc} \leq 0°$C, or $n_{ice} > 15\%$ and $T_{sfc} < T_{freeze}$, the surface is classified as ice, while if $n_{ice} < 15\%$ and $T_{sfc} > 0°$C ice-free conditions are assumed. Applying these criteria, 20% (30%) of the melt (freeze-up) cases remain unclassified; for these, camera images were additionally used. For melt season, 45% of the unclassified cases have $n_{ice} > 15\%$ and $T_{sfc} < 0°$C, while the images show ice-covered surfaces. For another 40%, substantial ice concentrations were found in the images and satellite products, but T_{sfc} was slightly positive ($\sim{<}1°$C). All of these cases are categorized as ice, while another $\sim5\%$ have $T_{sfc} > 0°$C, and the corresponding images show open water conditions. The remaining 10%, corresponding to 3% of the total summertime, generally fall

within the MIZ, where only a few ice floes are observed and $T_{freeze} < T_{sfc} < 0°$C. Because of the presence of ice, these cases are also included in the ice-condition category. For freeze-up, the images indicate open water for 75% of the initially unclassified cases, whereas the rest indicate mixed conditions (e.g., large open leads within larger-scale ice or MIZ) or newly formed thin ice. These periods, corresponding to 7% of autumn, are included in the ice-conditions category. Although the MIZ is a distinct surface state, neither open water nor ice-covered, and local conditions may be sensitive to the wind direction relative to the ice edge; classifying them as ice here does not introduce biases in our statistics because of short sampling time within the MIZ ($\sim5\%$). Finally, during the melt (freeze-up) season, 55% (65%) of the measurements were classified as ice and 45% (35%) as open water surfaces.

A drawback of this classification is that it does not account for variability of ice concentration. Concentrations between 80%–100% were found for 52% of melt and 21% of freeze-up cases, respectively. Lower concentration, 40%–80%, was found for 28% of the melting and 54% of the freeze-up period. These percentages are derived from SSMIS; AMSR2 gives similar statistics. This indicates that the ship track included a larger fraction of open leads during the later period. Furthermore, during the melt season, measurements were generally taken over thick multiyear ice, whereas during freeze-up the surface was sometimes covered with thin ice. Potential effects of these factors are discussed along with the results in section 3.

For our statistical analysis we use a 5-min time series for the surface state; near-surface meteorological, ocean surface, and remote sensing variables are averaged around these times. Lower-frequency data are also presented: 20-min-averaged turbulent fluxes and 6-hourly radiosonde profiles.

To identify temperature inversions in the radiosonde temperature profiles, we follow the methodology of Tjernström and Graversen (2009). We identify layers with a positive temperature gradient within the first 3 km, deeper than 20 m, and with inversion strength $>0.4°$C. Inversions separated by <100 m are merged. The strongest inversion in a radiosonde profile is also considered as the main inversion. When the main inversion has a base <100 m, it is classified as surface based, while a higher main inversion base is used as a proxy for planetary boundary layer (PBL) top. At least one temperature inversion is detected in 96% of the profiles.

Coexisting temperature and moisture inversions are considered an important feature for Arctic low clouds (Sedlar et al. 2012; Solomon et al. 2011). Hence, we also seek specific humidity inversion bases near main

temperature inversion bases and define humidity inversion boundaries similarly as described above. Moisture inversions with strengths $<0.2\,\mathrm{g\,kg^{-1}}$ are ignored (Nygård et al. 2014). Collocated inversions are present in 65% of the profiles.

Low-level wind speed maxima, commonly known as low-level jets (LLJs), can occur for several reasons: for example, as inertial oscillations after frictional decoupling at the surface (Andreas et al. 2000) or because of low-level baroclinicity (Langland et al. 1989), for example, associated with the ice edge. Many different criteria to detect LLJs are found in the literature (Stull 1988; Andreas et al. 2000; Baas et al. 2009). Here, we identify the LLJ core as a maximum in the wind speed in the lowest 3 km of the atmosphere, which is larger than $3\,\mathrm{m\,s^{-1}}$ and also exceeds the wind speed at the next minimum above (LLJ top) by both $2\,\mathrm{m\,s^{-1}}$ and 20%. A local minimum aloft is ignored if the wind speed above it increases less than $1\,\mathrm{m\,s^{-1}}$ before again decreasing to even lower values. If the wind speed above the jet core continuously decreases without a local minimum within the lowest 3 km, the lowest wind speed in the profile above the jet is taken as the LLJ top (Baas et al. 2009).

3. Results

All parameters are initially separated by season, and the seasonal categories are then further separated with respect to surface conditions: open water and sea ice. In this way, we attempt to isolate both seasonal features and the effect of the surface type. Results are often illustrated by relative frequency distributions (RFDs); although conclusions based on the mean statistics of an RFD are not representative of all the individual cases, this simple approach facilitates comparison between the different classes.

As a backdrop to the detailed results, it is interesting to first note that the transition from melt to freeze-up season was not gradual, as one might expect if it had been because of the gradual reduction in incoming solar radiation and a resulting cooling of the atmosphere from below. Instead, the transition was abrupt (Fig. 2) and appeared as a rapid cooling of the whole lower atmosphere. In addition to the gradual reduction in available solar energy, providing reduced surface warming, this allowed the surface to also lose heat by turbulent latent and sensible heat fluxes.

During ACSE, other studies conducted aboard the ship dictated the navigation to different areas at different times, and the sampling is likely affected by different regional weather patterns at different times. Hence, the rapid freeze-up may characterize only a specific region of the Arctic. Such abrupt seasonal transitions have been reported before in the Arctic (Sedlar et al. 2012; Persson 2012), but, to our knowledge, documented events are limited in number.

a. Surface and near-surface variables

The RFDs for T_{sfc} are presented in Figs. 3a and 3b. The long positive tail in the RFD for the melt season is partly due to *Oden*'s passage through the discharge from the Lena River, where T_{sfc} locally reached $\sim 7°C$. The T_{sfc} RFD for summer melt has an absolute peak near the melting point of freshwater ($\sim 0°C$), whereas during autumn freeze-up T_{sfc} peaks closer to the melting point of saline water ($\sim -2°C$). These peaks also correspond to the RFD peaks for the ice surface conditions. Open water T_{sfc} was mainly above $0°C$ during melt (Fig. 3a) and shifted toward cooler temperatures, mostly below $0°C$, in freeze-up (Fig. 3b).

During melt, the surface pressure P_{sfc} was less variable than in freeze-up (Figs. 3c,d), and the latter frequently experienced lower values ($\sim <1000\,\mathrm{hPa}$), indicating more synoptic-scale activity in freeze-up than in the melt season. To investigate the significance of these differences, we further examined the 5-min P_{sfc} anomalies relative to the mean P_{sfc} for the whole ACSE (not shown). Positive anomalies greater than one standard deviation are found in 14% of melt and 12% of freeze-up measurements (not shown), whereas corresponding negative anomalies were found in 2% and 37%, respectively. Hence, enhanced synoptic activity occurred in greater than one-third of the freeze-up period. The RFDs for the two surface types are similar for melt (Fig. 3c), whereas the peak in freeze is lower over ice than open water (Fig. 3d), suggesting that more fronts passed when *Oden* was in the ice.

The U_{10N} was generally also stronger during freeze-up than melt (Figs. 3e,f); the higher occurrence of wind speeds $>10\,\mathrm{m\,s^{-1}}$ (Fig. 3f) supports the hypothesis of more enhanced synoptic activity in this period than in melt season. The highest winds were more frequent over open water than over ice during summer melt (Fig. 3e), whereas the opposite is the case for autumn freeze-up (Fig. 3f); however, these differences may be due to insufficient sampling.

Finally, the near-surface atmosphere was close to saturation (with respect to water) in summer melt, almost independent of the surface state (Fig. 3g). Near saturation was also observed over ice-covered cases during freeze-up, whereas a less moist lower atmosphere often persisted over open water (Fig. 3h). High RH_w (RH with respect to liquid water) over sea ice, regardless of season, is consistent with Andreas et al. (2000), who concluded that atmospheric moisture over sea ice is always close to saturation, and with previous summer
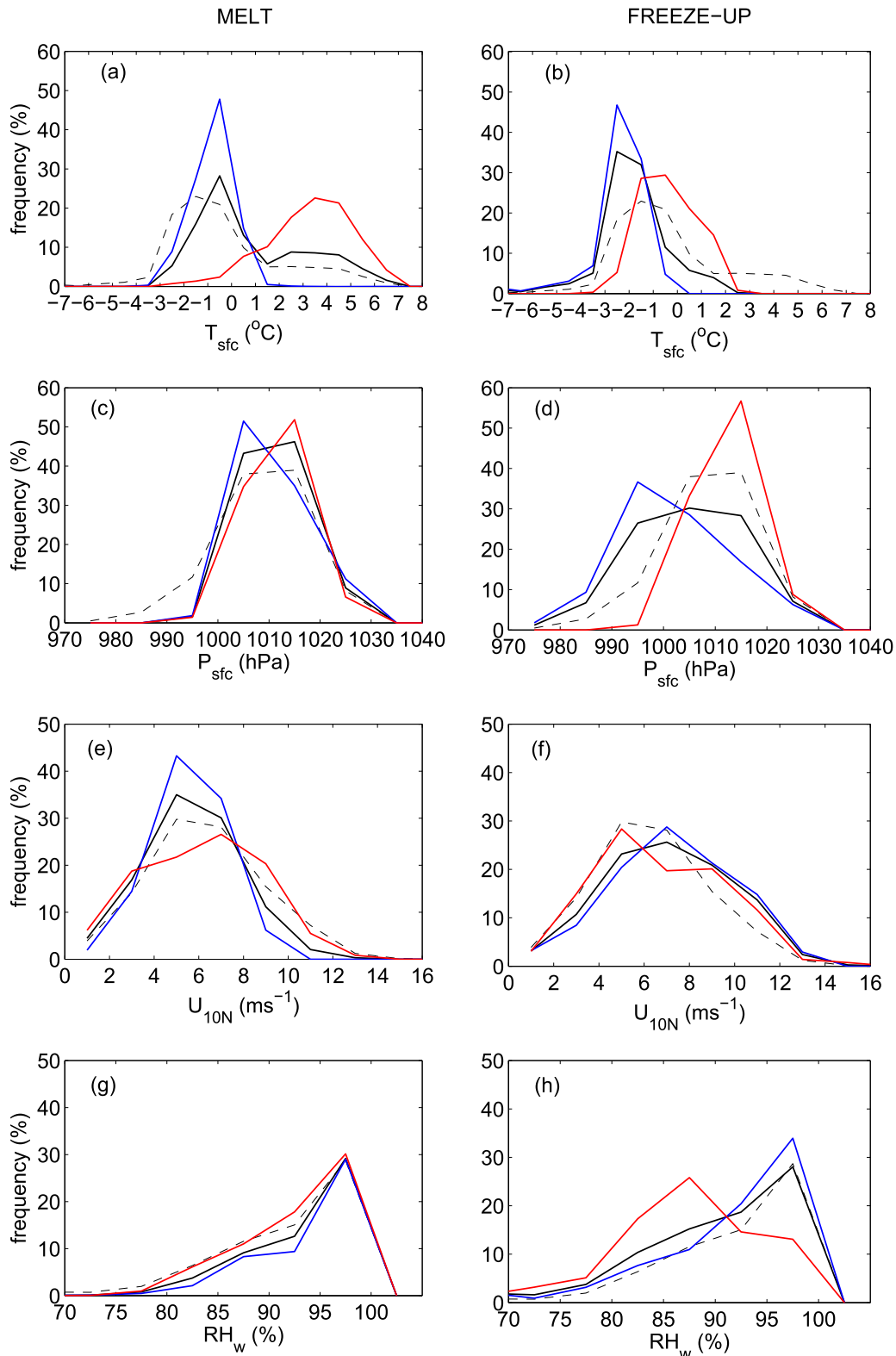
FIG. 3. RFDs of (a),(b) surface temperature T_{sfc} (°C); (c),(d) surface pressure P_{sfc} (hPa); (e),(f) 10-m neutral wind speed U_{10N} (m s^{-1}); and (g),(h) relative humidity with respect to liquid water RH$_w$ (%) at ~25 m for the (a),(c),(e),(g) melt and (b),(d),(f),(h) freeze-up season. Black solid lines give the total distribution for each season, whereas blue lines are for ice surface conditions and red for open water. Dashed black lines represent the RFDs for the whole experiment. Bins in all panels are centered in the interval.
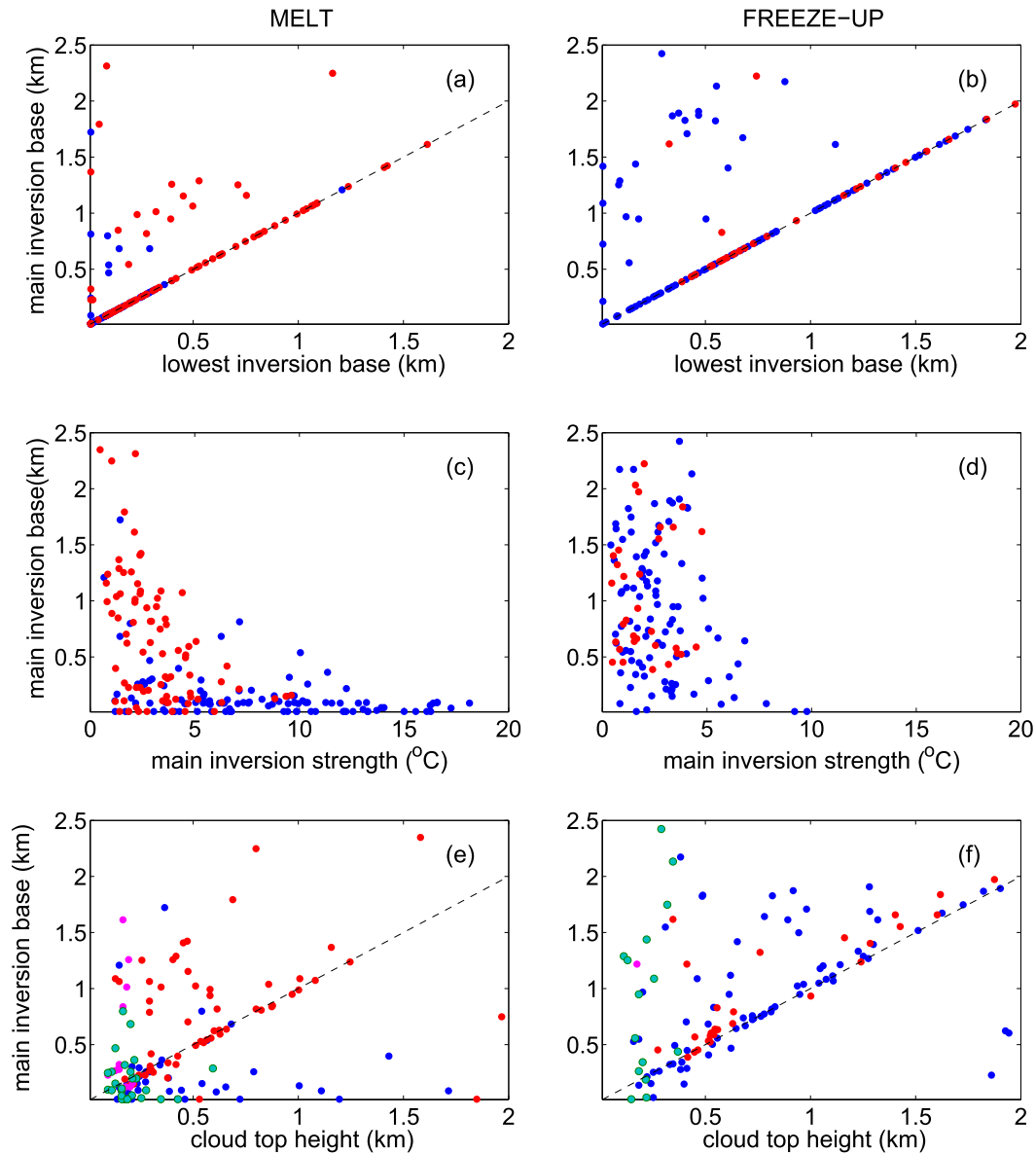
FIG. 4. Scatterplots of the heights (km) of the main inversion base heights against (a),(b) the heights (km) of the lower inversion base; (c),(d) the strengths (°C) of the main inversion; and (e),(f) the cloud-top heights for the (a),(c),(e) melt (b),(d),(f) freeze-up season. Blue (red) circles represent ice (open water) conditions. Fog-top heights are additionally shown in (e),(f) with green (pink) circles for ice (open water) conditions.

observations (Tjernström 2005; Tjernström et al. 2012). However, RH_w over open water (Fig. 3h) peaks at lower values compared to the other classes. A near-surface RH_w around 85% is typical for marine boundary layers (e.g., Heard et al. 2006), resulting from a balance between the surface flux over open water, precipitation, and entrainment of dry air near PBL top.

b. Temperature inversion characteristics

The relationships between temperature inversion-base, cloud-top, and fog-top heights are shown in

Fig. 4. Statistics of inversion-base heights, thicknesses, and strengths are additionally provided in Fig. 5. During melt, the strongest and lowest inversions coincided for 90% of the profiles over ice and for 72% over open water (Fig. 4a), indicating a strong link between PBL depth and the strongest inversion. The peak in the inversion-base RFD lies at the surface, with 40% of inversions being surface based, and the vast majority having a base <500 m (Fig. 5a). Furthermore, surface-based inversions most frequently occurred over ice (60%), whereas over open water
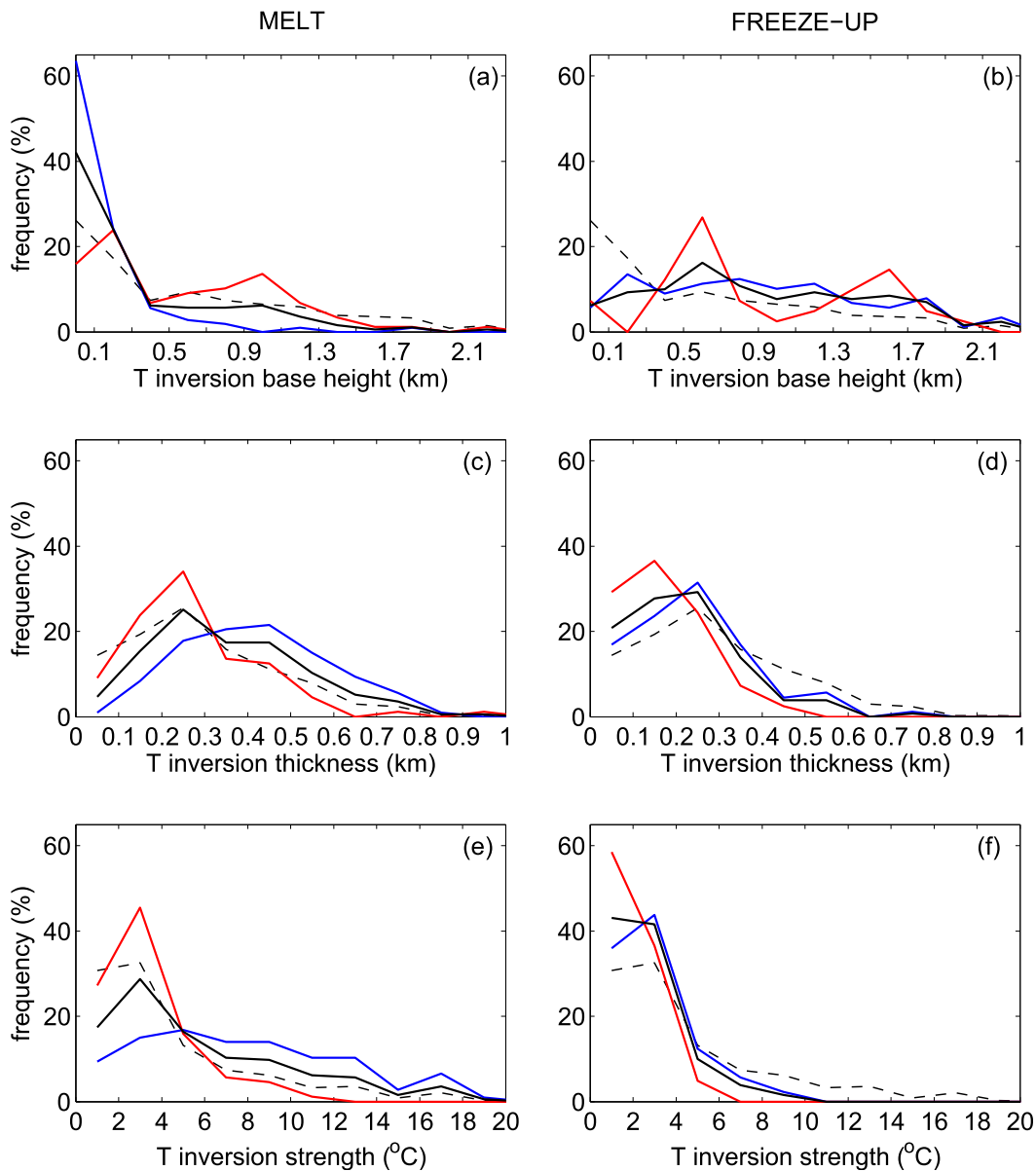
MELT   FREEZE−UP

FIG. 5. RFDs of the main inversion (a),(b) base heights (km); (c),(d) thicknesses (km); and (e),(f) strengths (°C), for the (a),(c),(e) melt and (b),(d),(f) freeze-up season. Inversion thickness is defined as the difference between inversion top and base heights. Inversion strength corresponds to the temperature difference between these levels. Line colors and bins are as in Fig. 3:

inversions were more usually elevated (Fig. 5a), indicating stronger vertical mixing consistent with higher surface temperatures (Fig. 3b). Cloud tops were usually higher than the inversion base over ice (Fig. 4e); cloud tops residing within the inversion layer are frequently observed in the Arctic and considered an important feature of this region (Sedlar et al. 2012). Over melting ice, there were also several cases of fog, often residing within the inversion (Fig. 4e). Conversely, over open water, cloud tops were frequently at

or below the inversion base (Fig. 4c), as in more prototypical marine stratocumulus, where the capping inversion is a combined consequence of cloud-top radiative cooling, turbulent mixing, and often subsidence (e.g., Bretherton et al. 2004).

Inversion strength is mainly determined by the surface conditions and advection above the PBL, along with turbulent mixing and cloud-top cooling. In Fig. 4c, greater inversion strengths generally coincided with surface-based inversions and occurred over ice. The

greatest magnitudes occurred during 29 July–8 August, when warm continental air was advected over melting sea ice, with a near-surface temperature close to the freshwater melting point while temperatures aloft reached ~19°C (Tjernström et al. 2015). Although statistics in Figs. 5c and 5e are likely skewed because of this event, the RFDs suggest that, for the bulk of the data, inversions were stronger and deeper over ice than over open water during the summer melt.

Freeze-up (Fig. 5b) was characterized by more elevated inversions and deeper PBLs than in summer melt, with no systematic difference with respect to the surface type. The main inversions were also the lowest for 74% of the time over ice and 81% over open water (Fig. 4b); thus, well-mixed PBLs were frequent in this season. A good correlation between cloud-top and inversion-base heights is found for the majority of the profiles, more so for open water than ice conditions (Fig. 4d). Inversions were weaker in autumn (Figs. 4d, 5f), with strengths rarely exceeding 5°C. The maximum inversion strength of ~10°C was reached during a short cloud-free period with a surface-based inversion (Fig. 4f). Although T_{sfc} was generally lower in autumn freeze-up than in summer melt (Figs. 3a,b), less than 10% of the inversions were surface based (Fig. 5b); the RFD is very broad, extending from 0 to >2 km. This is because the free troposphere was substantially colder in this season (Fig. 2a), setting the conditions for weaker inversions (Figs. 4d, 5f) than in summer (Figs. 4c, 5e). Thicker and stronger inversions over ice than over open water are also found in freeze-up (Figs. 5d,f), but these differences are less pronounced compared to summer melt (Figs. 5c,e).

Inversion characteristics are affected by both surface and large-scale conditions. We speculate that differences between melt and freeze-up are related to different synoptic weather patterns. However, within the same season, variable large-scale conditions may have occurred over ice and over open water; hence, attributing certain characteristics to the surface state alone may not be entirely trivial. Specifically, the extreme warming event documented in Tjernström et al. (2015) spans approximately one-third of the summer sea ice data. This obviously skews the statistics in Fig. 5; half of the surface-based inversions and all inversion strengths >12°C occurred in this period. Nevertheless, advection of warm air from adjacent ice-free areas (ocean or land) over a cooler surface layer is expected to occur frequently during Arctic melt season (Fig. 2a), as ACSE took place near the ice margin relatively far south and relatively close to the continent (Fig. 1). While warm air flows over the surface, the melting sea ice keeps its surface temperature diabatically locked at

the melting point (e.g., Persson et al. 2002; Persson 2012; Tjernström et al. 2015), resulting in persistent surface-based, strong inversions. Conversely, an open water surface is expected to respond faster to changes aloft. Hence, the inversion characteristics observed over summer ice are determined by *Oden*'s position relatively close to the ice edge, where advection events frequently occur, and by the melting state of the ice-covered surface.

c. Moisture inversion characteristics

Specific-humidity Q inversions coexisting with temperature inversions near cloud tops are an important source of moisture for low-level clouds (Sedlar et al. 2012; Solomon et al. 2011, 2014) and contribute to the high relative humidity in the Arctic PBL. Coexisting inversion layers were identified in 79% of the melt season profiles (86% over ice and 68% over open water) and in 44% of the freeze-up profiles (53% and 23%, respectively). During both seasons, T and Q inversions with collocated bases were found more frequently over ice than over open water. The higher frequency of T and Q inversion collocations over the summer ice is also consistent with the fact that cloud tops often lay within the inversion layer (Fig. 4e) in these cases.

In Fig. 6, statistics similar to Fig. 5 are presented, but for the Q inversions identified near the main temperature inversion. The RFDs in Fig. 6a are qualitatively very similar to those in Fig. 5a for T inversions for both surface types. This also holds for freezing ice conditions (Fig. 6b), whereas for freeze-up open water cases clear deviations are observed, with no Q inversion base near PBL top for PBL heights less than 700 m (Fig. 6b). In Figs. 6c and 6d, Q inversion thicknesses appeared somewhat deeper in melt than in freeze-up periods and also deeper over ice than open water, consistent with T inversions (Figs. 5c and 5d). However, Q inversions were systematically shallower than the corresponding T inversions in all cases (Figs. 5, 6), in agreement with previous results from ASCOS (Sedlar et al. 2012). Moisture inversions were generally stronger in melt than in freeze-up season (Figs. 6e and 6f); the strongest inversions were observed over the melting ice.

The low frequency of Q inversions near PBL top in the freeze-up period and the fact that, when they occurred, they were rather weak (especially over open water) indicate that clouds were generally not supported by entrainment of moisture above the PBL in this season. Such processes might be more important in summer and especially during ice-covered conditions, when advection of warmer and moister air played a critical role in shaping the lower atmosphere (see discussion in
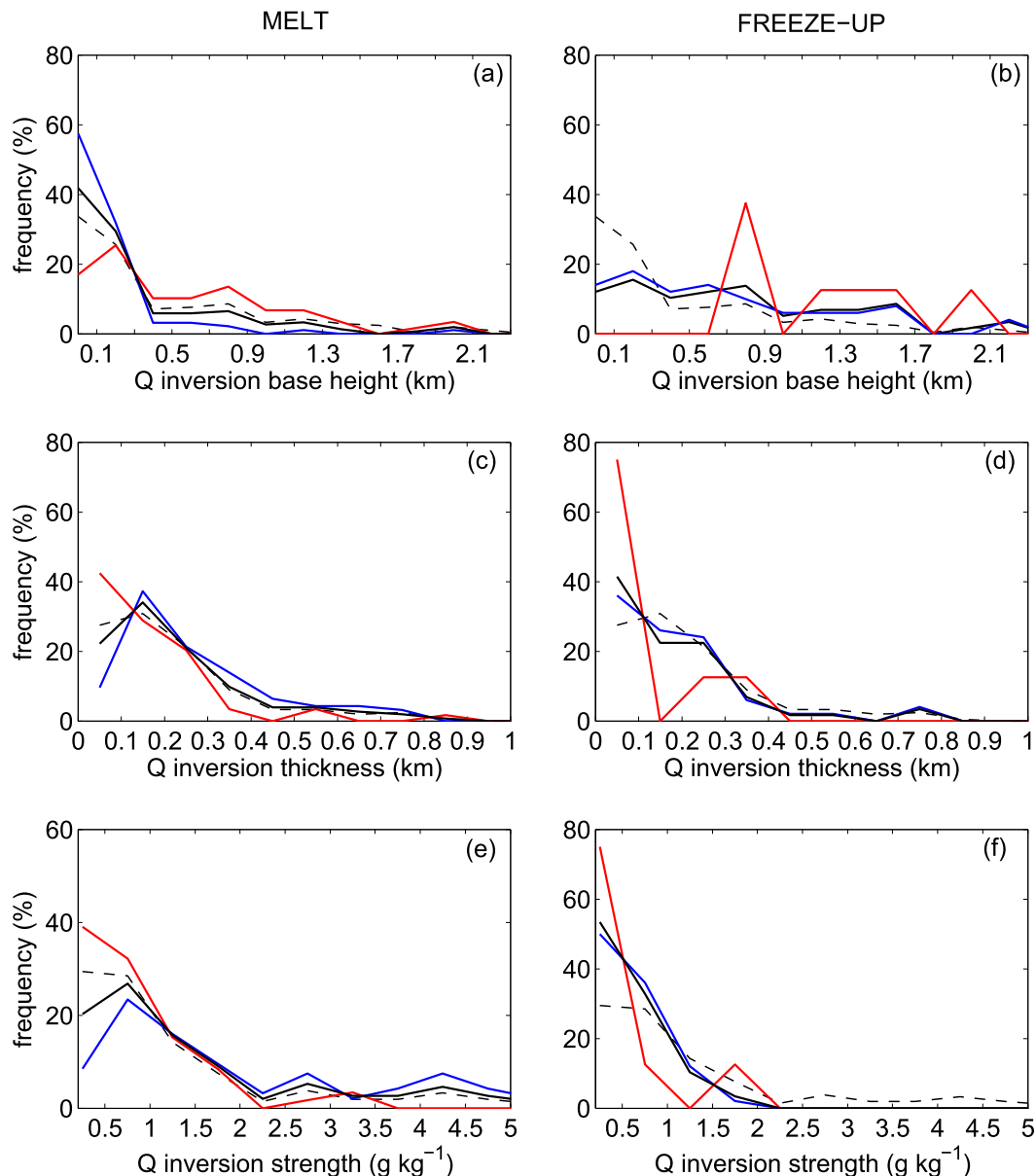
MELT　　　　　　　　　　　　　　　　FREEZE−UP

FIG. 6. As in Fig. 5, but for specific humidity inversions found to coexist with temperature inversions.

section 3b) and in supporting clouds within the surface-based stable layers.

d. Cloud characteristics

Clouds were frequent during ACSE; cloud cover <50% occurred only 5% of the time (4.5% for melt and 1.5% for freeze-up), whereas about ~90% of the 5-min averages for both seasons had a cloud cover ≥80%. Fog was more frequent during summer melt (~25%) and was twice as common over ice as over open water, compared with 7% during autumn freeze-up. Fog occurred under both surface-based and elevated T

inversions, and the mean fog-top height was ~200 m (also see Figs. 4e,f).

Figure 7 provides a statistical view of cloud geometry (excluding fog cases). Generally, low clouds dominated during the whole ACSE campaign, with cloud bases <200 m for about 50% of the time clouds were present (Figs. 7a,b). Such low clouds were more frequent in summer melt (~60%), with tops often <500 m (Fig. 7c): hence, only a few hundred meters thick (Fig. 7e). During this season, low and thin clouds dominated in ice-covered conditions (Figs. 7a,c), whereas clouds in ice-free conditions appeared more variable, often slightly
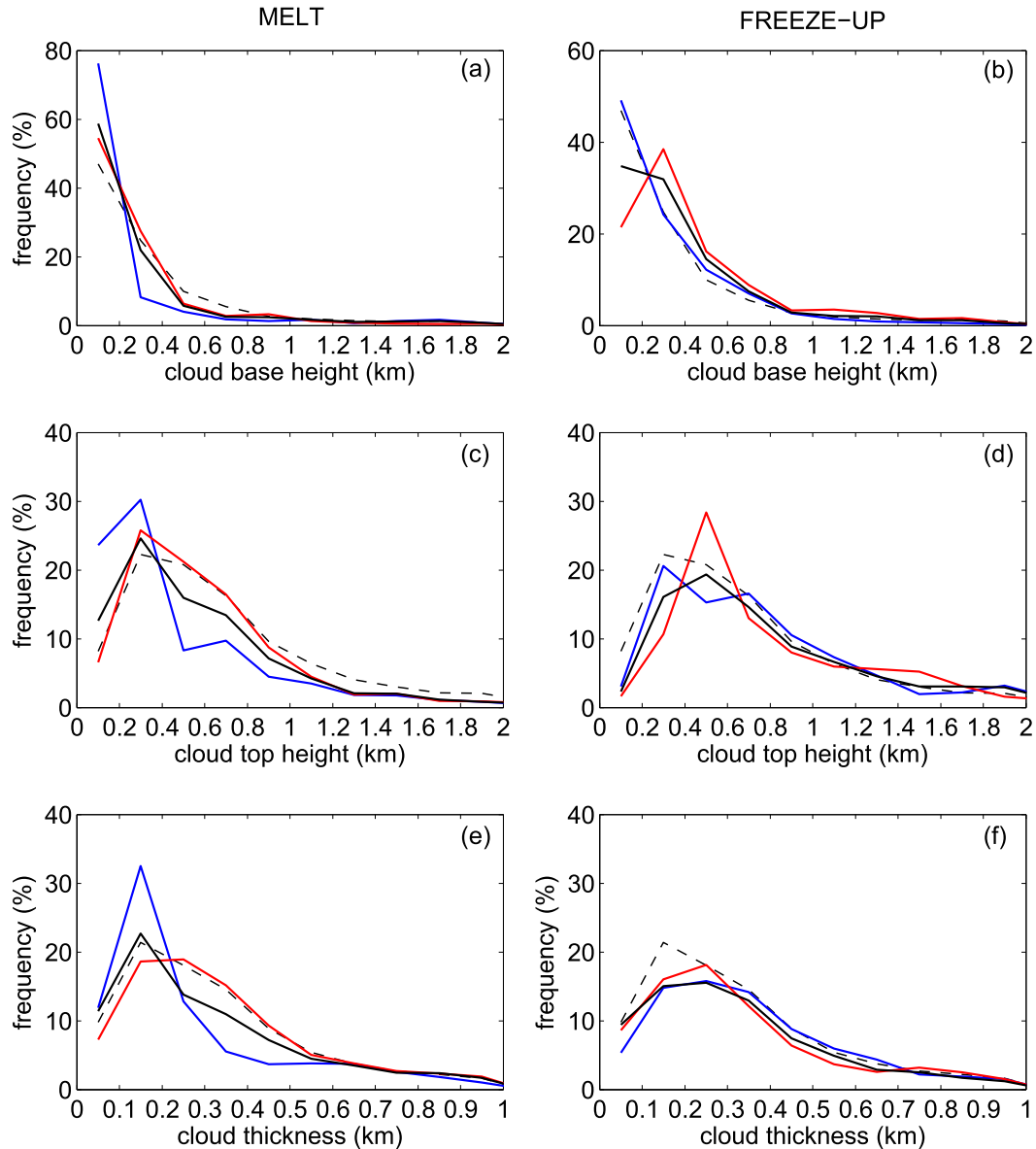
MELT

FREEZE-UP

FIG. 7. As in Fig. 5, but for (a),(b) cloud-base heights (km); (c),(d) cloud-top heights (km); and (e),(f) cloud thicknesses (km).

higher and thicker (Figs. 7c,e), consistent with the warmer surface (Fig. 3a). In autumn freeze-up, clouds were often somewhat higher (Figs. 7b,d) and deeper (Fig. 7f) compared to summer melt. Also, they were usually higher over ice-free than over ice-covered areas (Figs. 7b,d), but with no surface-type-related thickness difference (Fig. 7f). In general, autumn clouds were higher than summer clouds for the same surface conditions. Note that the lowest and thinnest clouds were associated with stable conditions (as over the summer ice), whereas somewhat thicker clouds were observed in all the other cases where deeper PBLs developed; either

over warmer water in summer or because of the relatively colder air aloft in autumn.

e. Surface fluxes

RFDs for friction velocity u_* normalized by U_{10N} and sensible and latent heat fluxes are shown in Fig. 8. Momentum flux is proportional to u_*^2, while scaling u_* with U_{10N} is the square root of the drag coefficient, which, to first order, depends on surface roughness. No seasonal difference in the scaled u_* is observed (Figs. 8a,b). However, it appears on average higher over ice than over open water. Sea ice has greater roughness than
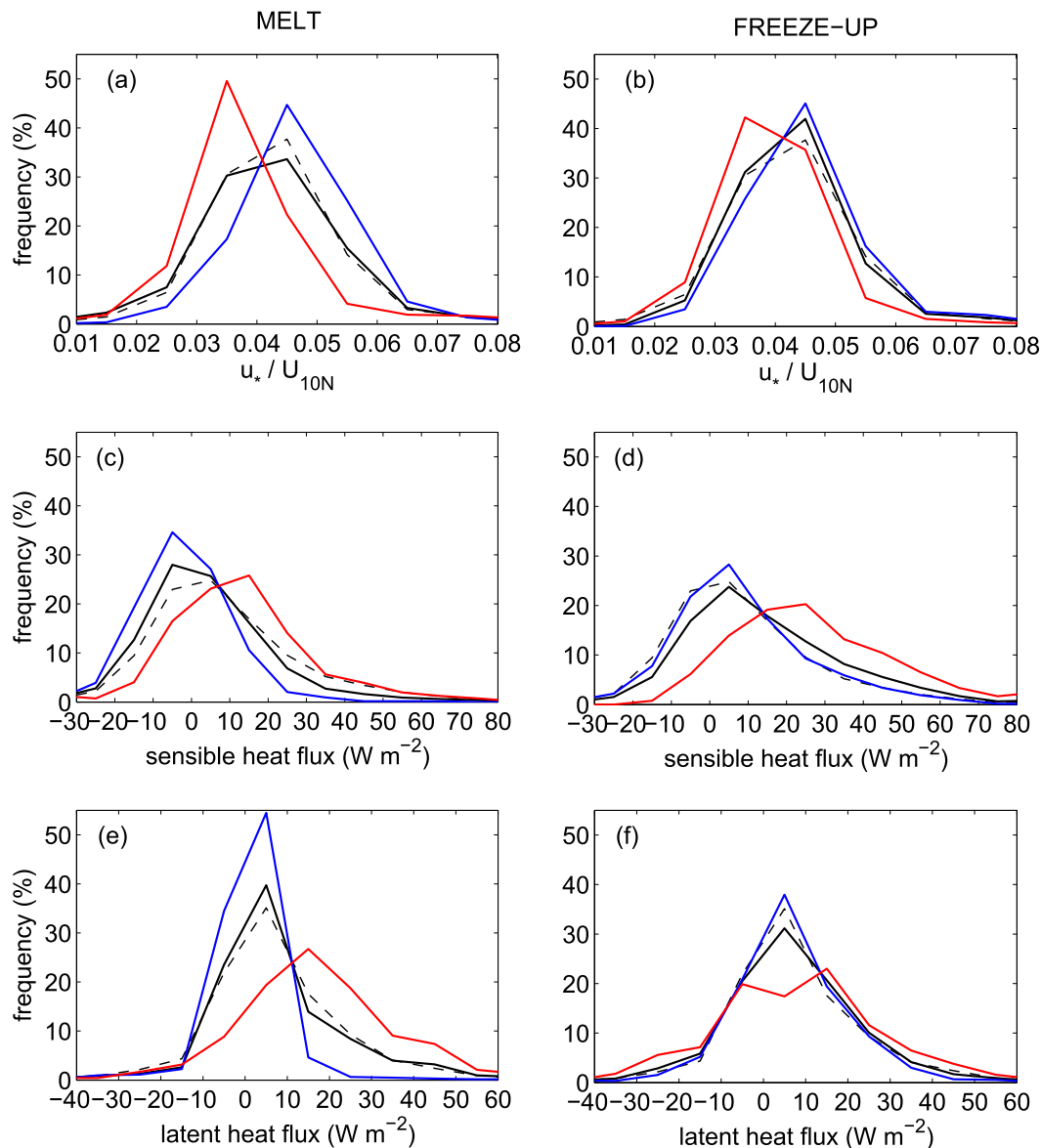
FIG. 8. As in Fig. 5, but for (a),(b) scaled friction velocity ($u_* U_{10N}^{-1}$); (c),(d) sensible heat flux (W m^{-2}); and (e),(f) latent heat flux (W m^{-2}). Positive heat fluxes are defined as upward.

open water (e.g., Elvidge et al. 2016); this difference is more pronounced in melt than in freeze-up, consistent with a larger fraction of new and smoother ice forming in the latter season.

Seasonal differences in sensible heat flux (Figs. 8c,d) are mainly due to the annual cycle of melt and freeze. In summer melt the atmosphere adds energy to the surface and melts ice, while the surface temperature cannot increase in response (Persson et al. 2002; Persson 2012; Tjernström et al. 2004). In autumn freeze-up the atmosphere is cooler and the sea surface loses heat and eventually freezes. Hence, the surface is cooling both from the changing radiation balance and by losing

sensible and latent heat by turbulent transfer. Consistent with the frequent presence of surface inversions, ice-covered surfaces during melt time were associated with a downward heat flux for about 60% of the time, most frequently between −10 and 0 W m^{-2} (Fig. 8c). Conversely, for ~70% of the freeze-up period, the heat flux remained upward over the ice, usually between 0 and 10 W m^{-2} (Fig. 8d). In both seasons, higher T_{sfc} over open water shifts the RFD toward more positive fluxes, compared to ice-covered surfaces. However, while open water T_{sfc} was much higher in summer melt (Figs. 3a,b), the atmosphere was much colder during freeze-up (Fig. 2), resulting in stronger upward heat

fluxes (Figs. 8c,d). This is consistent with the deeper PBLs (Fig. 5b) and generally higher clouds (Figs. 7b,d) over ice-free surfaces during freeze-up season.

The RFDs of latent heat fluxes for the two seasons have similar shapes (Figs. 8a,b). During summer melt and over ice, latent heat flux fluctuated near zero ($\pm 10\,W\,m^{-2}$), whereas over open water it was significantly larger and directed upward (Fig. 8e), as expected. Conversely, during autumn freeze-up the distributions of the latent heat flux for both surface types span similar ranges (Fig. 8f) and are also more variable compared to summer, indicated by the wider RFDs. The typically larger moisture fluxes over freezing than melting ice probably reflect both larger fractions of leads in the freeze-up season (also see section 2b for a discussion on ice concentrations) and the generally colder, and thus drier, atmosphere. Finally, one notable feature in both RFDs is that there appears to be relatively frequent occasions with negative values and condensation of water on the surface especially during autumn freeze-up, and also over melting ice.

In summary, heat and moisture fluxes give further indications about the processes that determine the boundary layer and cloud structure over the two surface types. The overall negative fluxes over the melting ice indicate frequent episodes of advection of warm and moist air over the cooler surface, resulting in surface-based inversions in both temperature and moisture. Advection was also the primary vapor source for cloud formation under these conditions. Over the summer open water, buoyancy fluxes from the warm surface supported the development of deeper PBLs and somewhat higher and thicker clouds. In autumn, the cooling of the atmosphere was the primary factor for the initiation of the freeze-up period, leading to turbulent heat loss at the surface over both ice and open water.

f. Thermal and dynamic vertical structure

Equivalent potential temperature Θ_E is a conserved property during moist adiabatic processes and hence is a good indicator of mixing. In section 3b we found that, for the vast majority of temperature profiles, the lowest and strongest inversions coincide. Therefore, either stably stratified or near-neutral well-mixed PBLs are expected as the most frequent thermal structures of the lower atmosphere. Information on vertical stability is shown in Fig. 9, with profiles of statistics of the Θ_E gradient plotted as a function of altitude, scaled by T inversion base and top heights.

In all panels, the T and Θ_E inversions generally coincide. Cases of shallower Θ_E than T inversions are found for the stable surface layers (Fig. 9a; red). This is related to the fact that the Q inversions were strong in these profiles but less deep than T inversions (Figs. 5, 6c). Hence, Θ_E inversions were, on average, stronger for

summer sea ice (Fig. 9a), and especially in cases with surface-based inversions, than for the other classes, consistent with previous discussions on the role of advection in these conditions. Near-zero gradients were generally observed in PBLs with elevated inversions in all panels, indicative of relatively well-mixed conditions. While very large gradients dominate in summer ice conditions (Fig. 9a; red boxes include 65% of summer ice cases), a well-mixed PBL is apparent in autumn freeze-up over both surface types (Figs. 9b,d).

The dynamic structure of the PBL is given in Fig. 10, showing vertical profiles of wind speed gradients. Stronger shear was generally observed during summer melt (Figs. 10a,c) than in autumn freeze-up (Figs. 10b,d), especially over sea ice, and for both surface-based and elevated inversion cases (Fig. 10a). This is consistent with a larger fraction of older, rougher ice and frequent stable stratification in summer melt and newly formed smooth ice with more well-mixed stratification in autumn freeze. Over open water in the melt season, several cases of strong shear near the surface are indicated in Fig. 10c, while the median gradients remain small. In contrast, the median wind speed gradient approaches zero rapidly above the surface for freeze-up time (Figs. 10b,d); a few cases of relatively strong shear can be found over freezing ice, whereas fewer cases were observed over open water.

LLJs were identified in 24% (21%) of the melt (freeze-up) period. During melt, 33% of the jet profiles were detected over open water and 67% (twice as often) over ice, while the corresponding frequencies in freeze-up were 53% and 47%, respectively. No significant differences with respect to surface conditions were found in the distributions of LLJ depths, strengths, and core heights (not shown); however, the total number of profiles is rather small. The structure of the wind speed profile appeared similar for both periods. Specifically, Figs. 11a and 11b reveal similar median wind profiles for summer and autumn jets, with winds usually being 65%–100% higher at the jet core than at the jet top. In both seasons, the jet maximum occurred within the lowest 500 m in 70% of the LLJ profiles (not shown).

One interesting seasonal feature was observed in the thermal structure encompassing the LLJs. In melt season, the profile shows a near-isothermal PBL extending to midway between surface and jet core height (Fig. 11c), capped by a temperature inversion, the top of which was usually close to the jet core. In contrast, during freeze-up LLJs usually had a more well-mixed thermal structure throughout the whole profile (Fig. 11d), extending through the jet core. As LLJs generated by an inertial oscillation typically have core heights close to the top of the stable boundary layer (Andreas et al. 2000), we speculate frictional decoupling
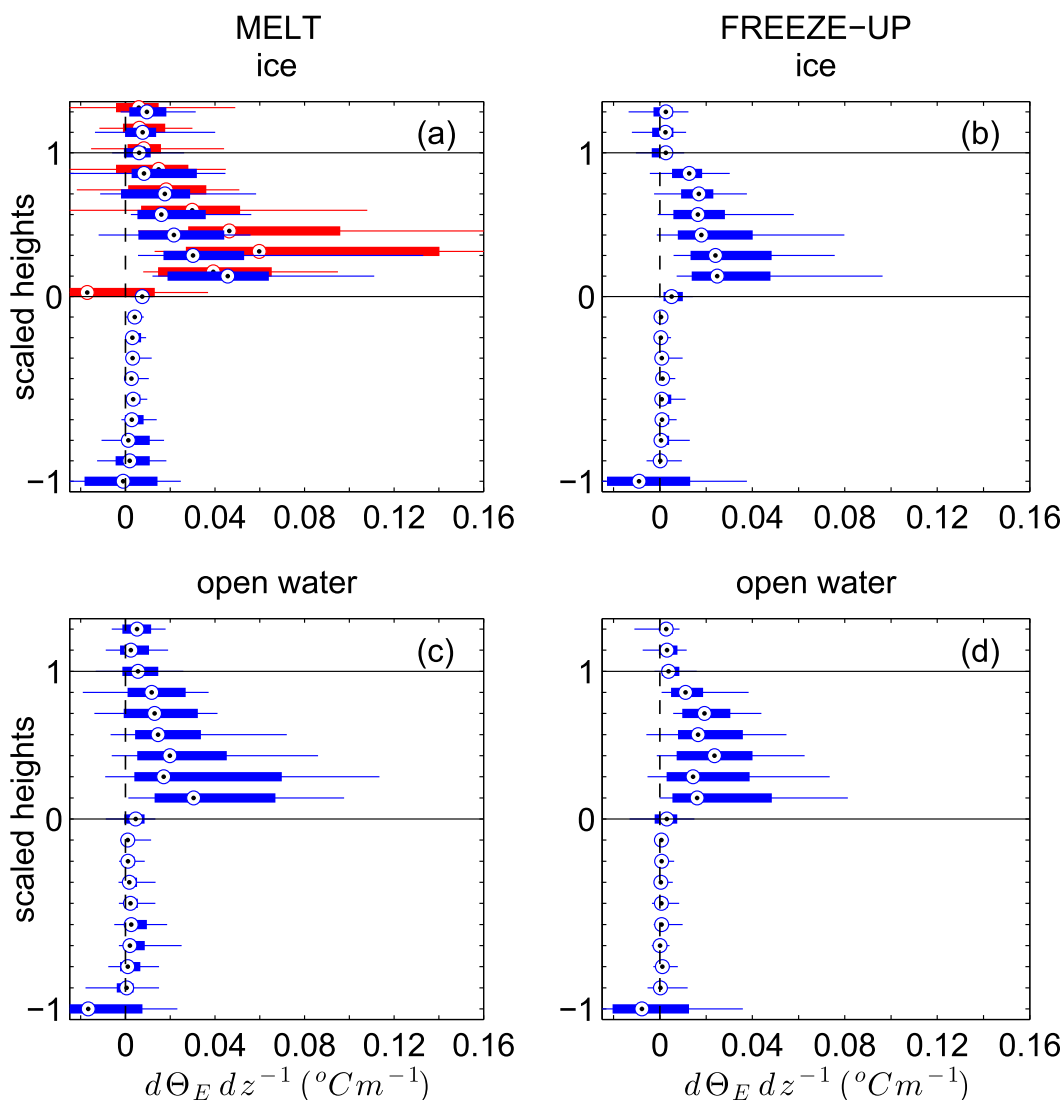
FIG. 9. Box-and-whisker profiles of equivalent potential temperature gradient $d\Theta_E/dz$ (°C m^{-1}) for the (a),(c) melt and (b),(d) freeze-up season, over (a),(b) ice-covered surface and (c),(d) open water. The red boxes in (a) represent profiles with a surface-based inversion. Heights are normalized so that -1, 0, and 1 represent surface, main inversion base, and main inversion top, respectively. In all panels, median values are indicated by white circles; edges of the box mark the lower and upper quartiles; and whiskers represent the 10th and 90th percentile. Red bars in (a) are slightly displaced upward to be distinguishable from the blue bars.

(Andreas et al. 2000) as the primary generation mechanism for summer jets. It is quite conceivable that advection of warm air over a cooler melting ice surface in summer could lead to a partial frictional decoupling. Other mechanisms may be more important during autumn freeze-up. The later season is characterized by more frontal passages, and fronts are also known to be a favorable environment for LLJ generation (Jakobson et al. 2013).

g. Cloud structure

Arctic clouds have a substantial impact on the surface energy budget, especially if they consist completely or partially of liquid droplets (Shupe and Intrieri 2004; Sedlar et al. 2011). Here, the microphysical structure of the lowest observed cloud layer is examined using statistics of Doppler radar moments.

Radar moments can be used to infer microphysical characteristics of the clouds. Radar reflectivity is primarily dependent upon particle size. When ice crystals are present, they tend to dominate the reflectivity since they are larger than droplets. Similarly, mean Doppler velocity can help distinguish hydrometeor phase (e.g., Shupe et al. 2005); small cloud droplets have a nearly negligible fall velocity, whereas larger ice crystals and rain drops fall
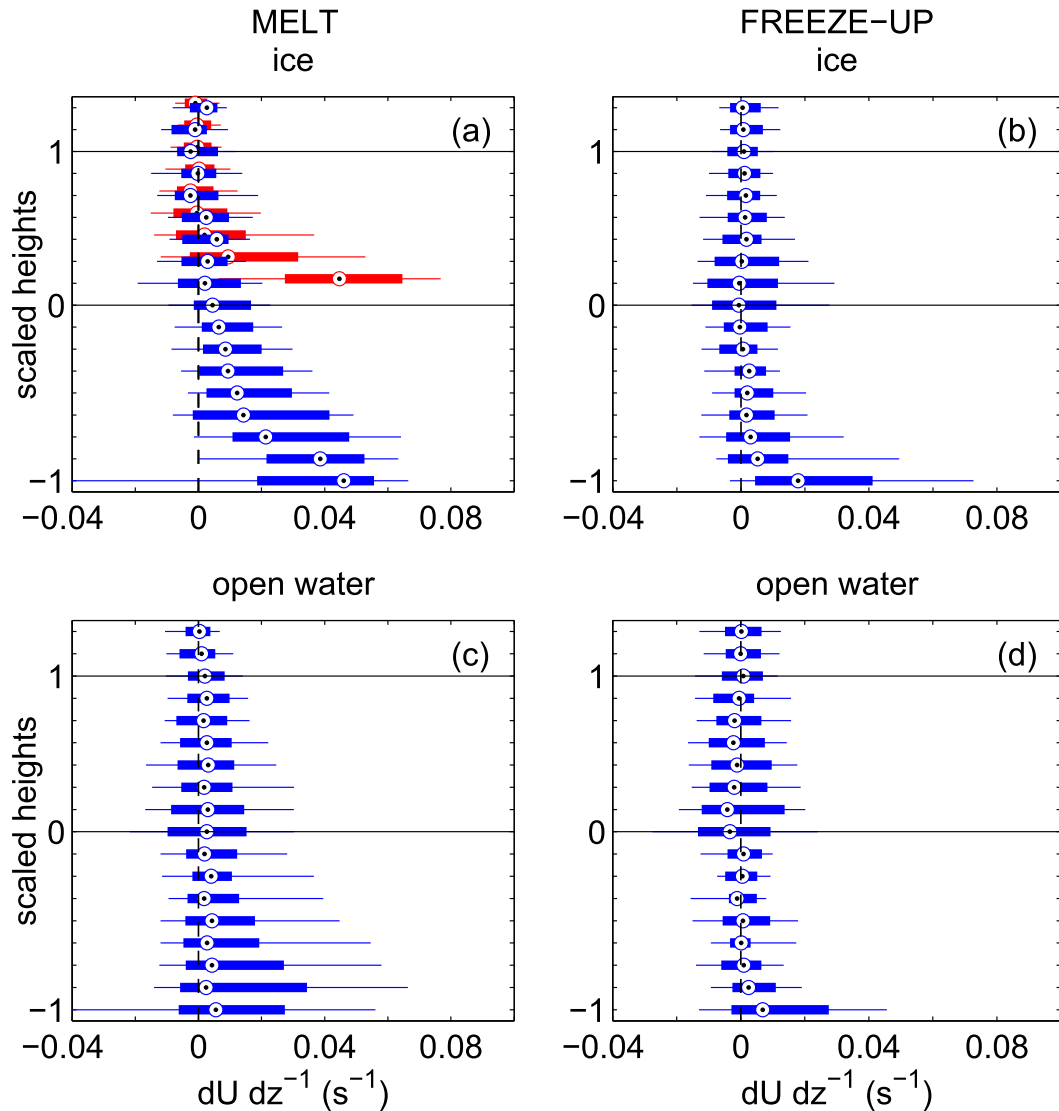
FIG. 10. As in Fig. 9, but for horizontal velocity gradients dU/dz (s^{-1}).

with a significant velocity; rain drops fall substantially faster than snow (e.g., Atlas 1990). Finally, the Doppler spectral width provides an indication of the spread in Doppler velocities of targets within a radar volume, which is related to hydrometeor size distribution and turbulence intensity. A radar volume containing a homogeneous hydrometeor size distribution will display a small spectral width if the turbulent-motion contributions are small, while a mixture of small liquid droplets and ice exhibits a relatively wide range of fall speeds, and hence the width of the Doppler spectrum will be relatively large (e.g., Shupe et al. 2004).

Box-and-whisker plots are used to illustrate the distribution of the radar mean moments within the cloud and subcloud layers (Figs. 12–14). Precipitating and nonprecipitating structures are analyzed separately,

since for the latter there are no radar signals below the cloud base. Radar returns below 158 m are discarded, as they are often contaminated by surface clutter; for clouds with bases below this level, lidar data are used to separate precipitating from nonprecipitating cases. Furthermore, clouds overlying fog layers with a fog top >~158 m are excluded from the analysis. As a result of these restrictions, only about 50 precipitating profiles over summer ice (0.05% of all radar profiles) pass the criteria; thus, statistics for this category are not presented. Nonprecipitating clouds over open water in autumn also have a small sample size (~5% of all radar profiles); this consists of ~30% autumn open water conditions. About 10% more nonprecipitating than precipitating cases were found over open water in summer melt, whereas for freeze-up ice conditions the
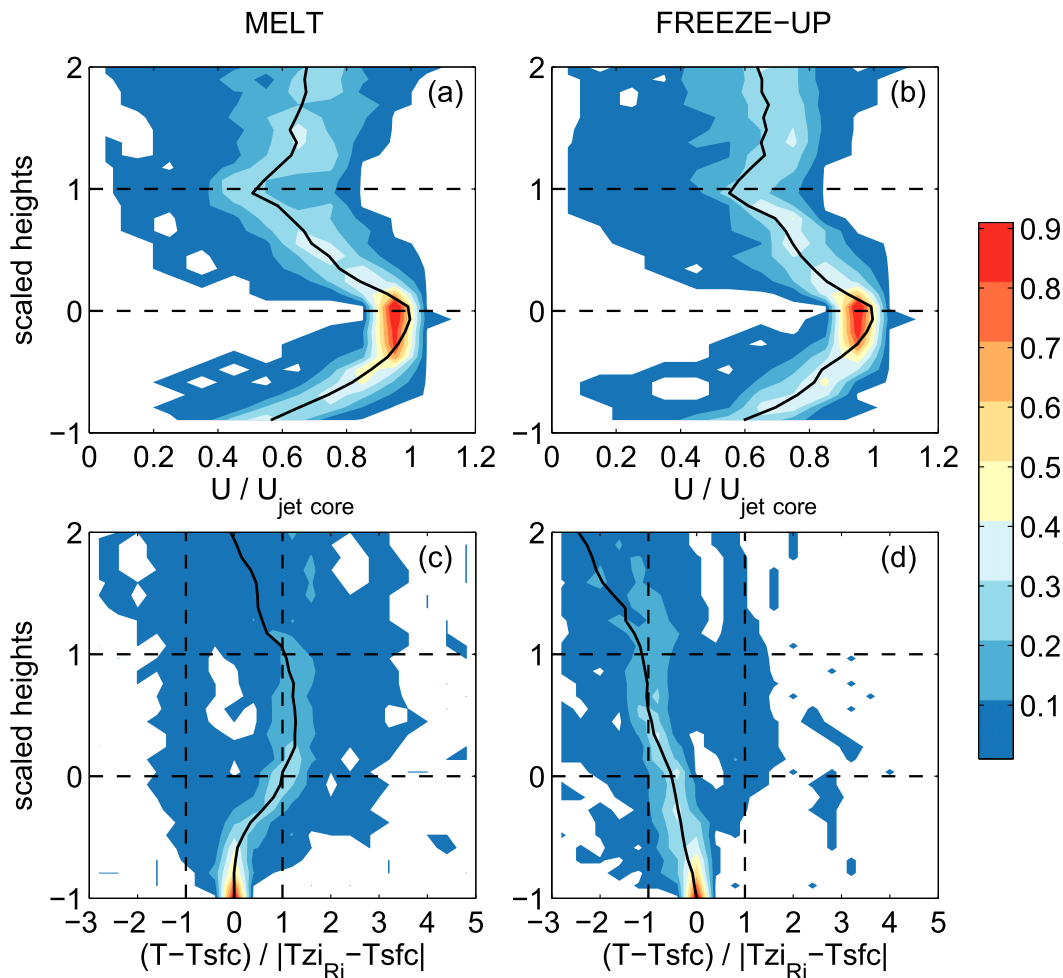
FIG. 11. RFD contour plots of scaled (a),(b) wind U (m s^{-1}) and (c),(d) temperature T (°C) profiles of low-level jets during the (a),(c) melt and (b),(d) freeze-up season. Temperature T is scaled by extracting the T_{sfc} and dividing with the absolute T difference between surface and Richardson mixing height z_{Ri}, which is considered as the top of the turbulent layer and is defined as the lowest height at which the gradient Richardson number $Ri_g \geq 0.4$ (Andreas et al. 2000; Jakobson et al. 2013). Thus, T is 0 at the surface and -1 or 1 at z_{Ri}; U is scaled with the jet core wind speed. Heights in all panels are normalized so that -1, 0, and 1 represent surface, jet core, and jet top height, respectively. Black solid lines represent the median profiles.

profiles were more equally distributed among the two subclasses. Another limitation in our method is that precipitation falling over different depths, whether reaching the surface or not, also affects the normalized precipitating profiles: for all four categories, the number of measurements included at each normalized height increases with height. Specifically, the boxes within the cloud level include about 40%–50% more values than those at the middle of the subcloud layer. During summer melt, precipitating clouds are usually found at very low altitudes. As a consequence, statistics at the lowest two normalized heights are based on <100 profiles; thus, they are not taken into account for the interpretation of the results. There is no optimal scaling method to apply on radar profiles that are

grouped by seasonal or surface criteria, as cloud properties and geometry can vary considerably. However, the applied method reveals useful information regarding the microphysical structures for the four different categories.

Figure 12 shows vertical profiles of radar reflectivity statistics. Reflectivity increases from cloud top to cloud base in precipitating clouds (Figs. 12b,d) during freeze-up, whereas during summer melt (Fig. 12c) cases with both increasing and decreasing in-cloud reflectivity are observed over open water, resulting in a more constant median profile. Increasing reflectivity suggests that in-cloud particles grew downward, probably through collision–coalescence for liquid drops or by deposition for ice crystals. Conversely, nonprecipitating cases generally
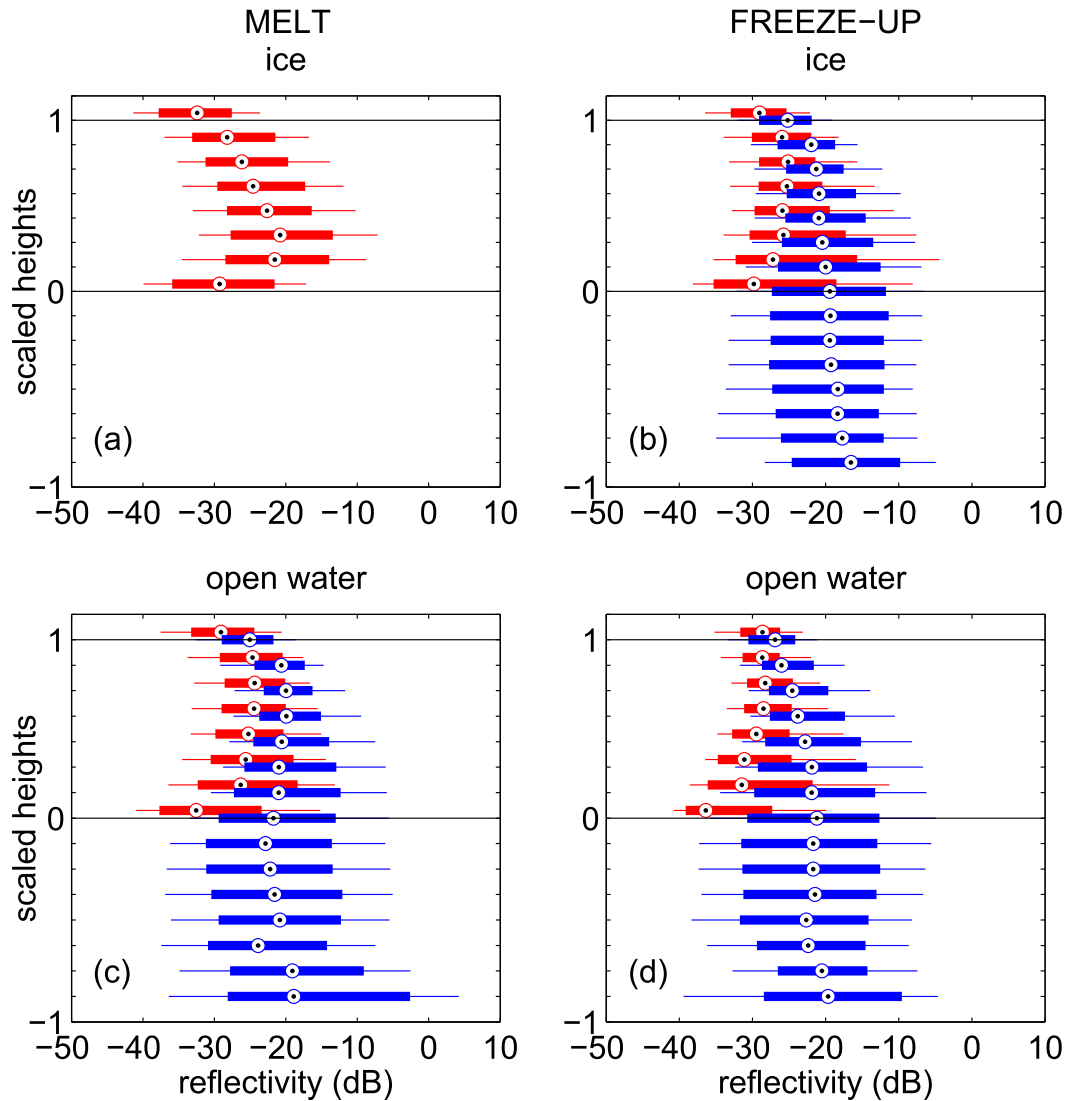
FIG. 12. Box-and-whisker profiles of Doppler radar reflectivity (dBZ) for the (a),(c) melt and (b),(d) freeze-up season, over (a),(b) ice-covered surface and (c),(d) open water. The blue (red) boxes represent precipitating (nonprecipitating) clouds. Heights are normalized so that -1, 0, and 1 represent surface, cloud base, and cloud top, respectively. Red bars in all panels are slightly displaced upward to be distinguishable from the blue bars.

showed a decrease in median reflectivity with decreasing height in the lower portion of the cloud. In Figs. 12b–d, these cases have systematically smaller magnitudes than the precipitating ones, since particles in these clouds did not grow to precipitation sizes.

Doppler velocities are generally smaller for nonprecipitating than for precipitating clouds (Figs. 13b–d), consistent with the smaller reflectivities (Figs. 12b–d). Moreover, in-cloud Doppler velocities increase from cloud top to cloud base for all precipitating cases. A slight increase with decreasing height is also observed in nonprecipitating cases in Figs. 13b and 13c, whereas the distributions in Figs. 13a and 13d are more homogeneous.

The velocity of the precipitation particles also continues increasing downward in the subcloud layer, indicative of an increase in particle characteristic size. The tails toward substantially larger velocities for open water cases in melt season (Fig. 13c) suggest occurrence of rain in this subset of cases, which occurred in generally warmer conditions (Fig. 2).

Precipitating clouds usually had wider spectral widths than nonprecipitating clouds (Figs. 14b–d), demonstrating the broadening effect due to a larger spread in particle sizes within a radar volume. The subcloud structure was similar for all of these subsets of data, with generally consistent spectral widths, except for the near-surface
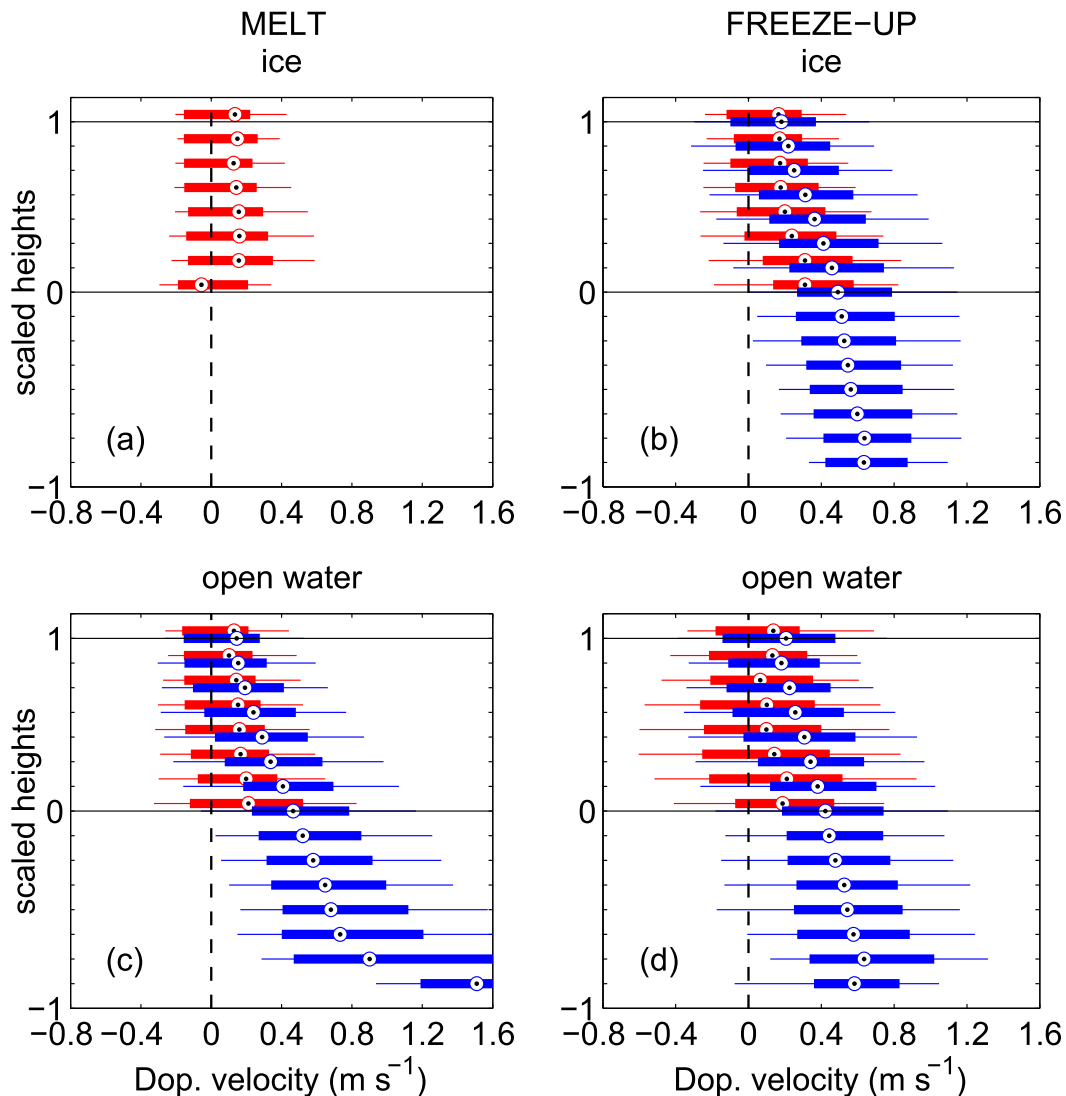
FIG. 13. As in Fig. 12, but for Doppler velocity (m s^{-1}).

layer (recall that the lower boxes correspond to low sample sizes for summer melt cases).

To further investigate the phase of each cloud type, in-cloud temperatures from radiosoundings are also analyzed. Summer clouds (Figs. 15a,c) had a median temperature around 0°C; the vast majority of in-cloud temperatures fell within the range from −2° to +3°C, indicating that these clouds likely lacked ice particles. Taking also the microphysical differences between nonprecipitating and precipitating cases into account for this season (Figs. 15a,c), one might conclude that the former were probably stratus clouds, consisting of smaller liquid particles, whereas the latter were more often optically thicker liquid stratiform or cumuliform clouds. In-cloud temperatures, on the other hand, were below 0°C (Figs. 15b,d) during autumn freeze-up, with a

median at about −5°C, suggesting that the formation of mixed-phase clouds was more likely. Finally, although certain deviations were observed in the microphysical structures between nonprecipitating and precipitating clouds in this season, in-cloud temperatures and lidar depolarization ratios (not shown) indicated the presence of ice crystals in both types. Hence, we assume that microphysical differences are due to different particle sizes: drizzle formation in the former cases and large crystals in the later.

4. Discussion

The delineation between the seasons was chosen based on atmospheric thermal structure, and the seasonal transition was surprisingly abrupt, rather than
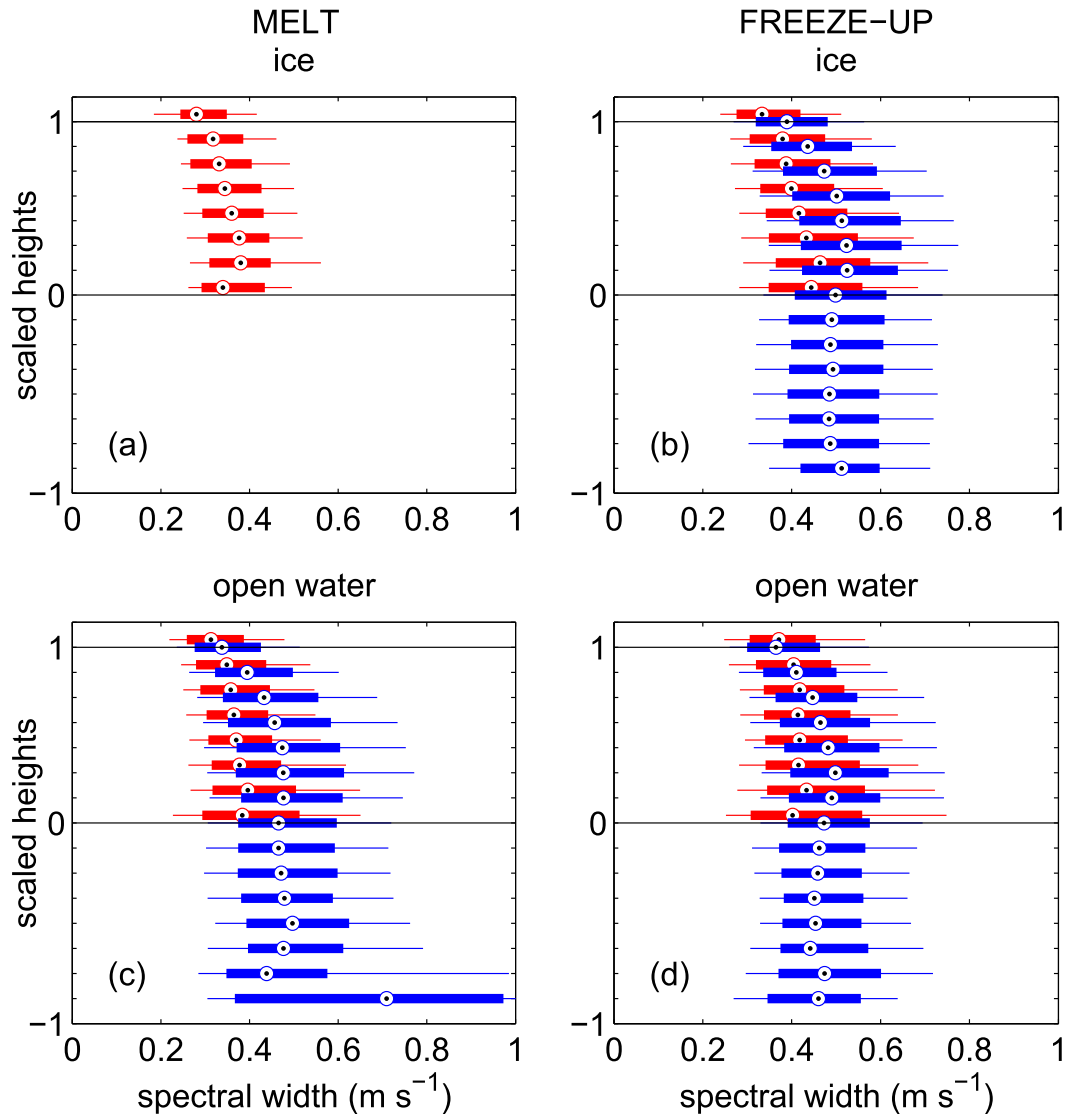
FIG. 14. As in Fig. 12, but for Doppler spectral width (m s^{-1}).

gradual, as would have been expected if it was primarily related to the change of net solar radiation. Moreover, the transition first took place in the atmosphere, and, even during periods when local freeze-up was observed, the surface remained warmer than the atmosphere. Hence the surface did not cool the air, as would have happened if the melt-to-freeze-up transition was controlled by the diminishing solar radiation. Instead the ocean warmed the near-surface air by an upward flux of sensible and latent heat; this enhanced the surface cooling and promoted formation of new sea ice. Synoptically driven seasonal transitions in the Arctic have been previously documented (e.g., Sedlar et al. 2011; Persson 2012), but these observations were within the ice pack, where changes in surface albedo, by precipitation or snowmelt, were responsible for changes in

the surface energy budget; here changes in the atmospheric circulation appear to be the primary factor.

In summer, atmospheric conditions over sea ice were characterized by frequent surface-based inversions. Two mechanisms dominate the formation of surface-based inversions (Bradley et al. 1992): first, a net-surface-radiation imbalance leading to surface cooling, which is expected to be common in Arctic winter; second, advection of warm air over a cooler surface layer, which is likely the primary factor here. While warmer air in summer was transported over the melting ice, its temperature was restricted to the melting point, causing a downgradient transport of sensible heat to the surface. In contrast, open water promoted elevated inversions, consistent with an upward heat flux from the surface. Therefore, inversions were systematically thicker and
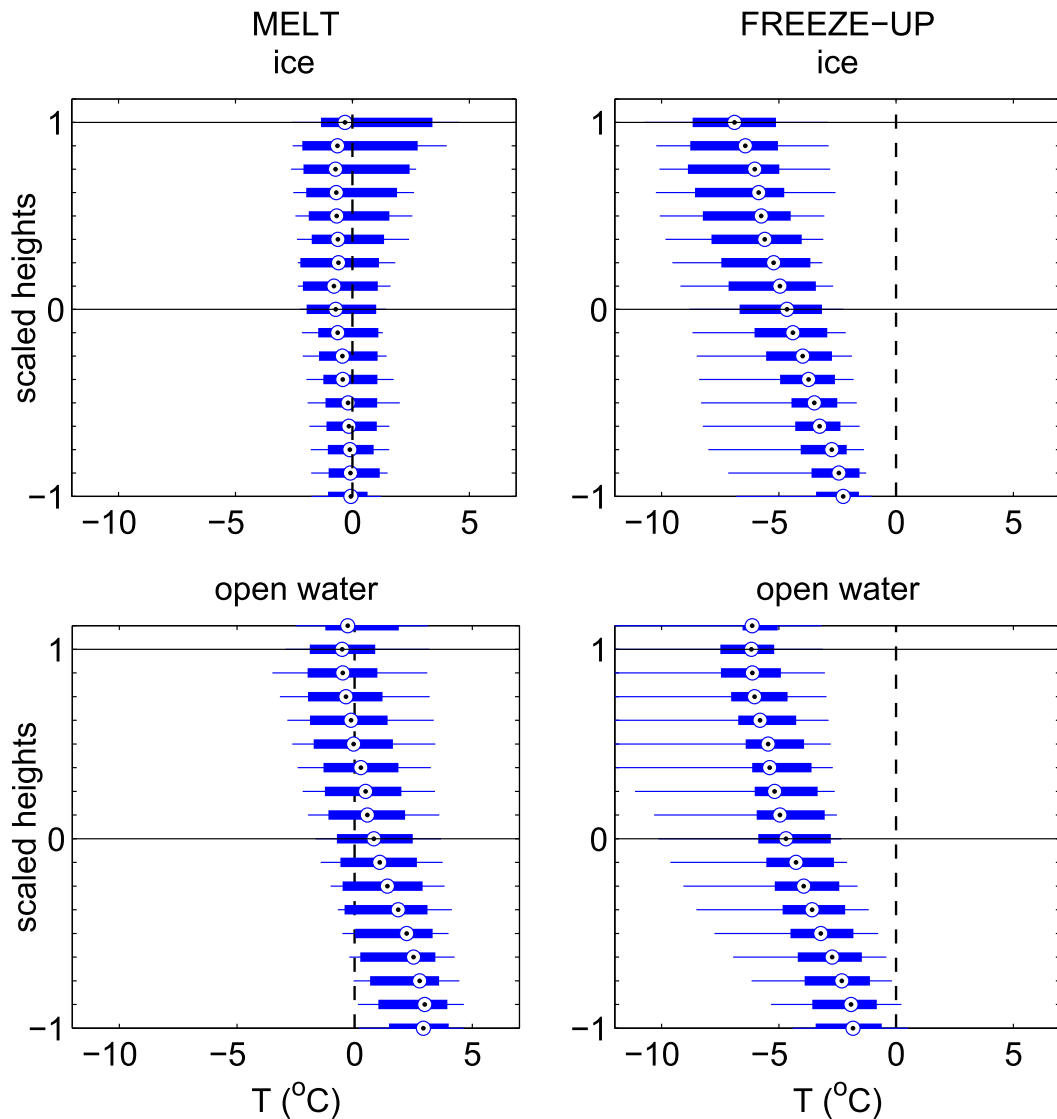
FIG. 15. Box-and-whisker profiles of temperature T (°C) for the (a),(c) melt and (b),(d) freeze-up season, over (a),(b) ice-covered surface and (c),(d) open water. Heights are normalized as in Fig 12.

stronger over ice than over open water, consistent with the concept of advection described above.

Our results are in contrast to previous studies, which found that the summer Arctic PBL over sea ice is most commonly well mixed with an elevated inversion (Serreze et al 1992; Tjernström and Graversen 2009; Zhang et al. 2011; Tjernström et al. 2012). We speculate that the reason for this difference is the fact that ACSE took place near the ice margin and relatively far south, with more pronounced effects of warm-air advection from adjacent ice-free areas (ocean or land), while most other studies were based on data from the interior Arctic ice pack or from land. Presumably, following this air farther downstream over the central Arctic Ocean, the

PBL would undergo a transformation to the well-mixed structure observed to dominate in several previous expeditions (e.g., SHEBA, AOE-2001, and ASCOS).

Another important PBL feature observed during summer melt was the frequent coexistence between moisture and temperature inversions (~80% of the time), which was more commonly found over ice-covered (~85%) than over ice-free surfaces (~70%). This signature, with increasing specific humidity across the top of clouds, is also consistent with the advection of warm and moist air over a substantially cooler surface discussed above.

Interestingly, differences in the lower-atmospheric structure between the two surface types are considerably

reduced in autumn freeze-up. Positive heat fluxes and elevated inversions, which on average were less deep and strong than in melt season, were observed over both ice and open water. A well-mixed PBL generally dominated throughout the whole period, while moisture inversions near PBL top were observed for less than 50% of the time and were rather weak. A decreasing frequency of temperature and humidity inversion coexistence from summer to autumn is consistent with pan-Arctic radiosounding analysis of such inversion structures (Nygård et al. 2014). PBL characteristics were likely determined by large-scale conditions, as advection of substantially colder air over a cold surface would induce instability and mixing; the partial absence of moisture inversions is also consistent with advection of cool and drier air over a warmer surface.

Finally, certain differentiations were also observed in cloud characteristics, depending on season or surface conditions. The relatively warm in-cloud temperatures in melt season indicate that summer clouds were more frequently liquid only; thin stratus clouds and fog frequently formed in ice conditions as a result of cooling of warm and moist air advected over melting sea ice, whereas buoyant mixing over open water favored the formation of liquid stratocumulus or cumulus clouds. Conversely, cold in-cloud conditions suggest that mixed-phase clouds dominated during freeze-up over both surface types. No pronounced differences were found in cloud characteristics and microphysical structure for this season.

Taylor et al. (2015) analyzed cloud profiles within different stability regimes and found a strong dependence between lower-tropospheric stability and cloud properties. Here, in melt season, ice and open water conditions fall within different stability regimes: the first was usually characterized by very high stability and the later by lower stability. In contrast, freeze-up cases generally fall within the same stability regime. This indicates that the pronounced differences in cloud properties between ice-covered and ice-free surfaces in summer melt may be primarily because of differences in atmospheric stability. Conversely, the lack of apparent differences in freeze-up can be explained by the similar stability conditions over the two surface types. Hence, cloud properties may primarily be affected by the atmospheric stability and secondarily by the surface conditions.

5. Conclusions

ACSE observations are used to investigate processes important for the structure of the Arctic lower troposphere by dividing the data according to surface type: sea ice or open water. The observations were taken from the summer melt into the early autumn freeze-up, allowing a further discrimination by season. A summary of our main findings is as follows:

- The initiation of autumn during ACSE was abrupt, indicating that it was not primarily driven by gradual changes in solar radiation. The thermal structure of the lower troposphere and enhanced synoptic activity suggest that this transition was associated with changes in the atmospheric circulation patterns.
- In summer, persistent surface-based inversions were observed over sea ice, associated with warm-air advection from adjacent open water or land over the melting ice. In contrast, elevated inversions were observed over open water as a result of positive buoyancy fluxes from the warm ocean surface. This distinction was not observed in autumn; elevated inversions associated with upward heat fluxes dominated over both surface types.
- In summer, fog and stratus clouds were frequently observed over the sea ice in episodes of warm, moist air advection events, while somewhat thicker stratocumulus and cumulus prevailed over the relatively warm open water surface; clouds were most frequently liquid only. Mixed-phase clouds emerged in autumn. This is in contrast to previous experiments over the central Arctic pack ice, finding mixed-phase clouds to be ubiquitous also in summer.
- LLJs occurred about 20%–25% of the time, summer and autumn alike. The thermal structure of the summer jets, with the jet core occurring near the top of the stable layer, indicates that inertial oscillations were causing these. The thermal jet structure in autumn was systematically different, suggesting a different mechanism.

Our findings indicate that understanding the processes that determine the transformation that the advected air mass undergoes while moving from open water, over the ice edge, and then further into the ice is important for an accurate representation of the Arctic PBL. The assumption here, based on results from ACSE and previous experiments, is that strong advection supports the persistence of the surface inversions near the MIZ and suppresses mixing by cloud radiative cooling, whereas, farther downstream into the central ice, cloud-driven turbulence would eventually overcome stability and lead to a well-mixed structure. Tjernström et al. (2015) illustrated a significant impact on the surface energy balance by this transition. Pithan et al. (2014) previously demonstrated how similar airmass transformations in winter could affect the surface temperature of the ice, and we argue that, although the processes are different, there may be a similar impact by summer airmass

transformation. However, further modeling and experimental studies of these processes are required.

Finally, the mechanisms controlling the abrupt transition between melt and freeze-up observed during ACSE need further exploration. The change was so abrupt in our data, despite the fact that the expedition was moving within the Chukchi Sea, that it must have had a regional impact. The pan-Arctic seasonal change is likely much more complicated, and the abruptness may disappear when averaging over the entire Arctic Ocean.

REFERENCES

Achtert, P., I. M. Brooks, B. J. Brooks, B. I. Moat, J. Prytherch, P. O. G. Persson, and M. Tjernström, 2015: Measurement of wind profiles by motion-stabilised ship-borne Doppler lidar. *Atmos. Meas. Tech.*, **8**, 4993–5007, doi:10.5194/amt-8-4993-2015.

Andreas, E. L, K. J. Claffey, and A. P. Makshtas, 2000: Low-level atmospheric jets and inversions over the western Weddell Sea. *Bound.-Layer Meteor.*, **97**, 459–486, doi:10.1023/A:1002793831076.

Atlas, D., Ed., 1990: *Radar in Meteorology*. Amer. Meteor. Soc., 806 pp.

Baas, P., F. C. Bosveld, H. Klein Baltink, and A. A. M. Holtslag, 2009: A climatology of nocturnal low-level jets at Cabauw. *J. Appl. Meteor. Climatol.*, **48**, 1627–1642, doi:10.1175/2009JAMC1965.1.

Barton, N. P., S. A. Klein, J. S. Boyle, and Y.-Y. Y. Zhang, 2012: Arctic synoptic regimes: Comparing domain-wide Arctic cloud observations with CAM4 and CAM5 during similar dynamics. *J. Geophys. Res.*, **117**, D15205, doi:10.1029/2012JD017589.

——, ——, and ——, 2014: On the contribution of longwave radiation to global climate model biases in Arctic lower tropospheric stability. *J. Climate*, **27**, 7250–7269, doi:10.1175/JCLI-D-14-00126.1.

Bintanja, R., R. G. Graversen, and W. Hazeleger, 2011: Arctic winter warming amplified by the thermal inversion and consequent low infrared cooling to space. *Nat. Geosci.*, **4**, 758–761, doi:10.1038/ngeo1285.

——, E. C. van der Linden, and W. Hazeleger, 2012: Boundary layer stability and Arctic climate change: A feedback study using EC-Earth. *Climate Dyn.*, **39**, 2659–2673, doi:10.1007/s00382-011-1272-1.

Bjornert, R., 1975: Field operations for the AIDJEX main experiment. *AIDJEX Bulletin*, No. 29, Arctic Ice Dynamics Joint Experiment, University of Washington, Seattle, Washington, 173–180.

Bradley, R. S., F. T. Keimig, and H. F. Diaz, 1992: Climatology of surface-based inversions in the North American Arctic. *J. Geophys. Res.*, **97**, 15 699–15 712, doi:10.1029/92JD01451.

Bretherton, C. S., and Coauthors, 2004: The EPIC 2001 stratocumulus study. *Bull. Amer. Meteor. Soc.*, **85**, 967–977, doi:10.1175/BAMS-85-7-967.

Carmack, E., and Coauthors, 2015: Toward quantifying the increasing role of oceanic heat in sea ice loss in the new Arctic. *Bull. Amer. Meteor. Soc.*, **96**, 2079–2105, doi:10.1175/BAMS-D-13-00177.1.

de Boer, G., and Coauthors, 2014: Near-surface meteorology during the Arctic Cloud Ocean Study (ASCOS): Evaluation of reanalyses and global climate models. *Atmos. Chem. Phys.*, **14**, 427–445, doi:10.5194/acp-14-427-2014.

Devasthale, A., M. Tjernström, M. Caian, M. A. Thomas, B. H. Kahn, and E. J. Fetzer, 2012: Influence of the Arctic Oscillation on the vertical distribution of clouds as observed by the A-Train constellation of satellites. *Atmos. Chem. Phys.*, **12**, 10 535–10 544, doi:10.5194/acp-12-10535-2012.

Edson, J. B., A. A. Hinton, K. E. Prada, J. E. Hare, and C. W. Fairall, 1998: Direct covariance flux estimates from mobile platforms at sea. *J. Atmos. Oceanic Technol.*, **15**, 547–562, doi:10.1175/1520-0426(1998)015<0547:DCFEFM>2.0.CO;2.

Ehrlich, A., E. Bierwirth, M. Wendisch, J.-F. Gayet, G. Mioche, A. Lampert, and J. Heintzenberg, 2008: Cloud phase identification of Arctic boundary-layer clouds from airborne spectral reflection measurements: Test of three approaches. *Atmos. Chem. Phys.*, **8**, 7493–7505, doi:10.5194/acp-8-7493-2008.

Elvidge, A. D., I. A. Renfrew, A. I. Weiss, I. M. Brooks, T. A. Lachlan-Cope, and J. C. King, 2016: Observations of surface momentum exchange over the marginal ice zone and recommendations for its parameterization. *Atmos. Chem. Phys.*, **16**, 1545–1563, doi:10.5194/acp-16-1545-2016.

Francis, J. A., and S. J. Vavrus, 2015: Evidence for a wavier jet stream in response to rapid Arctic warming. *Environ. Res. Lett.*, **10**, 014005, doi:10.1088/1748-9326/10/1/014005.

Guest, P. S., and K. L. Davidson, 1988: *MIZEX 87 Meteorology Atlas.* Naval Postgraduate School Tech. Rep. NPS-63-88-004, 140 pp. [Available online at http://hdl.handle.net/10945/28997.]

Heard, D. E., and Coauthors, 2006: The North Atlantic Marine Boundary Layer Experiment (NAMBLEX). Overview of the campaign held at Mace Head, Ireland, in summer 2002. *Atmos. Chem. Phys.*, **6**, 2241–2272, doi:10.5194/acp-6-2241-2006.

Jakobson, L., T. Vihma, E. Jakobson, T. Palo, A. Männik, and J. Jaagus, 2013: Low-level jet characteristics over the Arctic Ocean in spring and summer. *Atmos. Chem. Phys.*, **13**, 11 089–11 099, doi:10.5194/acp-13-11089-2013.

Jeffries, M. O., and J. Richter-Menge, Eds., 2015: The Arctic [in "State of the Climate in 2014"]. *Bull. Amer. Meteor. Soc.*, **96**, S169–S219.

Johannessen, O. M., 1987: Introduction: Summer marginal ice zone experiments during 1983 and 1984 in Fram Strait and the Greenland Sea. *J. Geophys. Res.*, **92**, 6717–6718, doi:10.1029/JC092iC07p06716.

——, and S. Sandven, 1989: SIZEX 89: A prelaunch ERS-1 ex-periment. SIZEX Group, Nansen Remote Sensing Center Experiment Rep. 23, 39 pp.

Kaleschke, L., C. Lüpkes, T. Vihma, J. Haarpaintner, A. Bochert, J. Hartmann, and G. Heygster, 2001: SSM/I sea ice remote sensing for mesoscale ocean–atmosphere interaction analysis. *Can. J. Remote Sens.*, **27**, 526–537, doi:10.1080/07038992.2001.10854892.

Karlsson, J., and G. Svensson, 2013: Consequences of poor repre-sentation of Arctic sea-ice albedo and cloud-radiation in-teractions in the CMIP5 model ensemble. *Geophys. Res. Lett.*, **40**, 4374–4379, doi:10.1002/grl.50768.

Klingebiel, M., and Coauthors, 2015: Arctic low-level boundary layer clouds: In situ measurements and simulations of mono- and bimodal supercooled droplet size distributions at the top layer of liquid phase clouds. *Atmos. Chem. Phys.*, **15**, 617–631, doi:10.5194/acp-15-617-2015.

Lampert, A., and Coauthors, 2012: The spring-time boundary layer in the central Arctic observed during PAMARCMiP 2009. *Atmosphere*, **3**, 320–351, doi:10.3390/atmos3030320.

Langland, R. H., P. M. Tag, and R. W. Fett, 1989: An ice breeze mechanism for boundary-layer jets. *Bound.-Layer Meteor.*, **48**, 177–195, doi:10.1007/BF00121789.

McFarquhar, G. M., and Coauthors, 2011: Indirect and semi-direct aerosol campaign: The impact of arctic aerosols on clouds. *Bull. Amer. Meteor. Soc.*, **92**, 183–201, doi:10.1175/2010BAMS2935.1.

Medeiros, B., C. Deser, R. Tomas, and J. Kay, 2011: Arctic in-version strength in climate models. *J. Climate*, **24**, 4733–4740, doi:10.1175/2011JCLI3968.1.

Moat, B. I., M. J. Yelland, and I. M. Brooks, 2015: Airflow dis-tortion at instrument sites on the *ODEN* during the ACSE project. National Oceanography Centre Internal Doc. 17, 114 pp. [Available online at http://eprints.soton.ac.uk/385311/.]

Moran, K. P., S. Pezoa, C. W. Fairall, C. R. Williams, T. E. Ayers, A. Brewer, S. P. de Szoeke, and V. Ghate, 2012: A motion-stabilized W-band radar for shipboard observations of marine boundary-layer clouds. *Bound.-Layer Meteor.*, **143**, 3–24, doi:10.1007/s10546-011-9674-5.

Nygård, T., T. Valkonen, and T. Vihma, 2014: Characteristics of Arctic low-tropospheric humidity inversions based on radio soundings. *Atmos. Chem. Phys.*, **14**, 1959–1971, doi:10.5194/acp-14-1959-2014.

Persson, P. O. G., 2012: Onset and end of the summer melt season over sea ice: Thermal structure and surface energy perspective from SHEBA. *Climate Dyn.*, **39**, 1349–1371, doi:10.1007/s00382-011-1196-9.

——, C. W. Fairall, E. L Andreas, P. S. Guest, and D. K. Perovich, 2002: Measurements near the Atmospheric Surface Flux Group tower at SHEBA: Near-surface conditions and surface energy budget. *J. Geophys. Res.*, **107**, 8045, doi:10.1029/2000JC000705.

Pinto, J. O., and J. A. Curry, 1995: Atmospheric convective plumes emanating from leads: 2. Microphysical and radiative processes. *J. Geophys. Res.*, **100**, 4633–4642, doi:10.1029/94JC02655.

Pithan, F., and T. Mauritsen, 2014: Arctic amplification dominated by temperature feedbacks in contemporary climate models. *Nat. Geosci.*, **7**, 181–184, doi:10.1038/ngeo2071.

——, B. Medeiros, and T. Mauritsen, 2014: Mixed-phase clouds cause climate model biases in Arctic wintertime temperature inversions. *Climate Dyn.*, **43**, 289–303, doi:10.1007/s00382-013-1964-9.

Prytherch, J., M. J. Yelland, I. M. Brooks, D. J. Tupman, R. W. Pascal, B. I. Moat, and S. J. Norris, 2015: Motion-correlated flow dis-tortion and wave-induced biases in air–sea flux measurements

from ships. *Atmos. Chem. Phys.*, **15**, 10 619–10 629, doi:10.5194/acp-15-10619-2015.

Sedlar, J., and Coauthors, 2011: A transitioning Arctic surface energy budget: The impacts of solar zenith angle, surface al-bedo and cloud radiative forcing. *Climate Dyn.*, **37**, 1643–1660, doi:10.1007/s00382-010-0937-5.

——, M. D. Shupe, and M. Tjernström, 2012: On the relationship between thermodynamic structure and cloud top and its cli-mate significance in the Arctic. *J. Climate*, **25**, 2374–2393, doi:10.1175/JCLI-D-11-00186.1.

Serreze, M. C., and J. A. Francis, 2006: The Arctic amplifica-tion debate. *Climatic Change*, **76**, 241–264, doi:10.1007/s10584-005-9017-y.

——, and R. G. Barry, 2011: Processes and impacts of Arctic am-plification: A research synthesis. *Global Planet. Change*, **77**, 85–96, doi:10.1016/j.gloplacha.2011.03.004.

——, J. D. Kahl, and R. C. Schnell, 1992: Low-level temperature inversions of the Eurasian Arctic and comparisons with Soviet drifting station data. *J. Climate*, **5**, 615–629, doi:10.1175/1520-0442(1992)005<0615:LLTIOT>2.0.CO;2.

Shupe, M. D., and J. M. Intrieri, 2004: Cloud radiative forcing of the Arctic surface: The influence of cloud properties, surface al-bedo, and solar zenith angle. *J. Climate*, **17**, 616–628, doi:10.1175/1520-0442(2004)017<0616:CRFOTA>2.0.CO;2.

——, P. Kollias, S. Y. Matrosov, and T. L. Schneider, 2004: De-riving mixed-phase cloud properties from Doppler radar spectra. *J. Atmos. Oceanic Technol.*, **21**, 660–670, doi:10.1175/1520-0426(2004)021<0660:DMCPFD>2.0.CO;2.

——, T. Uttal, and S. Y. Matrosov, 2005: Arctic cloud microphysics retrievals from surface-based remote sensors at SHEBA. *J. Appl. Meteor.*, **44**, 1544–1562, doi:10.1175/JAM2297.1.

——, V. P. Walden, E. Eloranta, T. Uttal, J. R. Campbell, S. M. Starkweather, and M. Shiobara, 2011: Clouds at Arctic at-mospheric observatories. Part I: Occurrence and macro-physical properties. *J. Appl. Meteor. Climatol.*, **50**, 626–644, doi:10.1175/2010JAMC2467.1.

Solomon, A. S., M. D. Shupe, P. O. G. Persson, and H. Morrison, 2011: Moisture and dynamical interactions maintaining de-coupled Arctic mixed-phase stratocumulus in the presence of a humidity inversion. *Atmos. Chem. Phys.*, **11**, 10 127–10 148, doi:10.5194/acp-11-10127-2011.

——, ——, ——, ——, T. Yamaguchi, P. M. Caldwell, and G. de Boer, 2014: The sensitivity of springtime Arctic mixed-phase stratocumulus clouds to surface layer and cloud-top inversion-layer moisture sources. *J. Atmos. Sci.*, **71**, 574–595, doi:10.1175/JAS-D-13-0179.1.

Sotiropoulou, G., J. Sedlar, R. Forbes, and M. Tjernström, 2016: Summer Arctic clouds in the ECMWF forecast model: An evaluation of cloud parametrization schemes. *Quart. J. Roy. Meteor. Soc.*, **142**, 387–400, doi:10.1002/qj.2658.

Spreen, G., L. Kaleschke, and G. Heygster, 2008: Sea ice remote sensing using AMSR-E 89-GHz channels. *J. Geophys. Res.*, **113**, C02S03, doi:10.1029/2005JC003384.

Stroeve, J. C., T. Markus, L. Boisvert, J. Miller, and A. Barrett, 2014: Changes in Arctic melt season and implications for sea ice loss. *Geophys. Res. Lett.*, **41**, 1216–1225, doi:10.1002/2013GL058951.

Stull, R. B., 1988: *An Introduction to Boundary Layer Meteorology.* Kluwer Academic, 666 pp.

Svensson, G., and J. Karlsson, 2011: On the Arctic wintertime cli-mate in global climate models. *J. Climate*, **24**, 5757–5771, doi:10.1175/2011JCLI4012.1.

Taylor, P. C., S. Kato, K.-M. Xu, and M. Cai, 2015: Covariance between Arctic sea ice and clouds within atmospheric state

regimes at the satellite footprint level. *J. Geophys. Res. Atmos.*, **120**, 12 656–12 678, doi:10.1002/2015JD023520.

Tjernström, M., 2005: The summer Arctic boundary layer during the Arctic Ocean Experiment 2001 (AOE-2001). *Bound.-Layer Meteor.*, **117**, 5–36, doi:10.1007/s10546-004-5641-8.

——, and R. G. Graversen, 2009: The vertical structure of the lower Arctic troposphere analysed from observations and the ERA-40 reanalysis. *Quart. J. Roy. Meteor. Soc.*, **135**, 431–443, doi:10.1002/qj.380.

——, C. Leck, P. O. G. Persson, M. L. Jensen, S. P. Oncley, and A. Targino, 2004: The summertime Arctic atmosphere: Meteorological measurements during the Arctic Ocean Experiment 2001. *Bull. Amer. Meteor. Soc.*, **85**, 1305–1321, doi:10.1175/BAMS-85-9-1305.

——, and Coauthors, 2005: Modelling the Arctic boundary layer: An evaluation of six ARCMIP regional-scale models using data from the SHEBA project. *Bound.-Layer Meteor.*, **117**, 337–381, doi:10.1007/s10546-004-7954-z.

——, J. Sedlar, and M. D. Shupe, 2008: How well do regional climate models reproduce radiation and clouds in the Arctic? *J. App. Meteorol. Climatol.*, **47**, 2405–2422, doi:10.1175/2008JAMC1845.1.

——, and Coauthors, 2012: Meteorological conditions in the central Arctic summer during the Arctic Summer Cloud Ocean Study (ASCOS). *Atmos. Chem. Phys.*, **12**, 6863–6889, doi:10.5194/acp-12-6863-2012.

——, and Coauthors, 2014: The Arctic Summer Cloud Ocean Study (ASCOS): Overview and experimental design. *Atmos. Chem. Phys.*, **14**, 2823–2869, doi:10.5194/acp-14-2823-2014.

——, and Coauthors, 2015: Warm-air advection, air mass transformation and fog causes rapid ice melt. *Geophys. Res. Lett.*, **42**, 5594–5602, doi:10.1002/2015GL064373.

Uttal, T., and Coauthors, 2002: Surface heat budget of the Arctic Ocean. *Bull. Amer. Meteor. Soc.*, **83**, 255–276, doi:10.1175/1520-0477(2002)083<0255:SHBOTA>2.3.CO;2.

Verlinde, J., and Coauthors, 2007: The Mixed-Phase Arctic Cloud Experiment. *Bull. Amer. Meteor. Soc.*, **88**, 205–221, doi:10.1175/BAMS-88-2-205.

Vihma, T., and Coauthors, 2014: Advances in understanding and parameterization of small-scale physical processes in the marine Arctic climate system: A review. *Atmos. Chem. Phys.*, **14**, 9403–9450, doi:10.5194/acp-14-9403-2014.

Wesslén, C., M. Tjernström, D. H. Bromwich, G. de Boer, A. M. L. Ekman, L.-S. Bai, and S.-H. Wang, 2014: The Arctic summer atmosphere: An evaluation of reanalyses using ASCOS data. *Atmos. Chem. Phys.*, **14**, 2605–2624, doi:10.5194/acp-14-2605-2014.

Zhang, Y., D. J. Seidel, J.-C. Golaz, C. Deser, and R. A. Tomas, 2011: Climatological characteristics of Arctic and Antarctic surface-based inversions. *J. Climate*, **24**, 5167–5186, doi:10.1175/2011JCLI4004.1.